Source parameter estimation after attenuation correction through the use of Q tomography

Pasquale De Gori (corresponding author): pasquale.degori@ingv.it
INGV, via di Vigna Murata 605, 00143, Rome.

Francesco Pio Lucente: pio.lucente@ingv.it
INGV, via di Vigna Murata 605, 00143, Rome.

Claudio Chiarabba: claudio.chiarabba@ingv.it
INGV, via di Vigna Murata 605, 00143, Rome.

Abstract

The measurement of earthquake source parameters is affected by large uncertainties, and different approaches lead to large variability in results. One crucial aspect is the trade-off between attenuation (Q) and corner frequency (fc) in spectral fitting: the source corner frequency, inversely proportional to the fault size, can be severely masked by attenuation and site effects. In this paper we describe a method to solve the trade-off based on the fit of displacement spectra to find the source characteristics (corner frequency, fc and the signal moment Ωo) and the single station attenuation operator (t*), in addition to the site response. We follow a parametric approach based on the use of 3D Q seismic tomography and a bootstrap–based method for selecting the best spectra fit. The correction of attenuation with synthetic values derived by 3D attenuation tomography efficiently deals with the trade-off between source and path terms, leading to small uncertainties in the determination of source unknowns (fc and signal moment Ωo), thus yielding constrained estimates of source parameters for low- to medium-magnitude earthquakes.

We show an application to the Emilia 2012 seismic sequence, for which we computed the source parameters for 1240 aftershocks (from an initial data-set of 1748) with local magnitude ranging from 2.0 to 4.7 by using the spectral fit from P and S waves. About 80 % of stress drop estimations are characterized by relatively low uncertainties (within 20% of the estimated values), with maximum values of about 40% for the remaining 20%. The attenuation correction is effective to determine source parameters for small magnitude earthquakes, hence we obtain reliable estimates of source parameters for the entire aftershock sequence. This approach gives the opportunity to infer the mechanical state of a complete fault system by taking advantage of the larger number of low magnitude events (with respect to the largest ones) that always follow a major earthquake.

Introduction

The determination of seismic source parameters (seismic moment, source dimension, stress drop) play an important role in studying earthquake physics, for example to define fault interaction or to predict the ground shaking (i.e Boore 1983). Following the basic theoretical relationship that relates static stress drop to seismic moment and source dimension (Eshelby, 1957; Brune, 1970; Kanamori and Anderson, 1975), their computation may appear a trivial task. However, reliable estimation of source parameters remains problematic, leading to controversial assumptions about the source scaling of earthquakes. It is commonly accepted that, for large earthquakes, seismic moment scales with fault dimension and stress drop remain almost constant (Aki, 1967; Stein and Wysession, 2002).

Conversely, for small- to moderate-size events, different views have been argued. Some authors suggested that stress drop increases with the size of earthquakes (e.g. Mayeda and Walter, 1996; Mayeda et al., 2007) while others conclude that self-similarity holds even for small magnitude events (e.g Abercrombie, 1995; Imanishi and Ellsworth, 2006). Therefore, a large variability persists in source parameter studies that arise from the determination of source dimensions and the correction of the observed signal for attenuation and site effect.

In fact, in the far field approximation, the observed seismograms or, equivalently, the shape of the observed spectral amplitudes, are the results of the interaction of three contributes: i) the source, ii) the along-path attenuation and iii) the site response (i.e. Stein and Wysession, 2002).

To perform source analysis, the observations (seismograms or spectra) must be "cleaned" of terms ii) and iii) and, under the assumption that the shape of the fault is rectangular or circular (Kanamori and Anderson, 1975), the event seismic moment, the source dimension and the static stress drop (called static source parameters) are usually computed.

One big problem in obtaining reliable measurements deals with the correction for path attenuation and site response that are in trade-off with source terms (Boatwright et al., 1991; Ko et al., 2011; Zollo et al., 2014; Abercrombie 2021). Different approaches are adopted to address this issue. Abercrombie (2021) made a wide and complete review of all the methods currently used to face this problem and to estimate source parameters, describing the assumptions and the limitations of each method.

Here, we synthesize some crucial aspects for a comparison with the methodology we adopted.

One strategy in use to correct path, site and the frequency dependence of attenuation relies on the Empirical Green Function (EGF) from seismic events with similar locations (e.g. Hough 1997; Hough 2001; Ide et al., 2003; Imanishi and Ellsworth 2006). Given a couple of events, close in space but with a considerable difference in magnitudes (see for details Abercrombie 2021), the smallest event acts as EGF for the more energetic one. This approach requires that earthquakes are co-located and significantly different in size (Abercrombie, 2015, 2021), with impact on the applicability for a limited dataset of events. Further applications of EGF methods are based on the spectral stacking of large number of events occurred in clusters or at larger scale to isolate the source terms (e.g. Prieto et al., 2004; Shearer et al., 2006; Allmann and Shearer, 2007; Trugman and Shearer, 2017). Generally, the removal of path effects with spectral ratio requires some assumption on attenuation homogeneity within the rock volume.

Recently, Yoshimitsu et al., 2019 (hereinafter YEA), proposed a method based on the coda wave spectral ratios between a large magnitude event and a small event acting as EGF. The stacks of all the spectral ratios are used to extract the two corner frequencies of the couple of events and their

moment ratio. This method gives robust estimation of stress drop and reliable uncertainty measurements.

An alternative approach is to filter the path and site terms by a spectral inversion scheme, using either a non-parametric or parametric approach. The main difference is the correction used for the attenuation term. In a non-parametric scheme, the attenuation term is computed by a model that, for each analyzed frequency, consists in a smooth function of distance obtained by inverting the spectral observations (e.g., Bindi et al., 2004; Oth et al., 2008; Oth et al., 2011, Picozzi et al., 2017). In the parametric approach, the attenuation and the source model are used as a-priori information (e.g. Edwards et al., 2008). The attenuation term is computed in a three-dimensional tomographic model that constrain the geometry and the spatial variability of the Q structure (Rietbrock, 2001, Edwards et al., 2008; Koulakov et al. 2011) leading to more realistic attenuation corrections with respect to a uniform Q model (Lees and Lindley, 1994; Tsumura et al., 2000; Rietbrock, 2001).

In this paper, we developed a methodology that follows this latter parametric approach, where, in a multi-step calculation scheme, the output of each step is used as input for the next step.
The first part of our procedure relies on the fit of P- and S-waves observed spectra as described in Stachnick et al. (2004), where all the spectra of one event are simultaneously used to find the source characteristics (fc and seismic moment) and single stations attenuation decays. In the second part, we compute a 3D attenuation structure for P- and S-waves by using a 3D velocity model and 3D earthquake locations as described in Rietbrock (2001). In the last part, the attenuation factors computed in the Qp and Qs tomographic model are used to correct the spectra and to find the source parameters by using P- and S-waves separately.
Furthermore, we compare our S-wave fc estimations with those derived by applying the method of YEA, where coda wave spectral ratios are used. We apply both our method and the YEA method to the aftershocks sequence of the 2012 Emilia earthquakes (Scognamiglio et al., 2012) using the seismograms recorded at local distances by the permanent and temporary stations deployed in the epicentral area (Govoni et al., 2014).

General Formulae from Theory

The far field velocity spectrum, $V_{ij}(f)$, observed at a station (*i-th*) from the earthquake *j-th* is the result of different physical processes occurring at the source, along the ray-path and at the recording site.

These different contributions in the frequency domain are expressed by multiplicative terms (e.g., Scherbaum, 1990):

$$V_{ij}(f) = 2\pi f \cdot S_i(f) \cdot A_{ij}(f) \cdot R_j(f) \cdot I_j(f) \qquad (1)$$

where S_i is the source spectrum of the i-th event; A_{ij} is the attenuation term; R_j is the site response dependent on the shallow geology structure beneath the recording site; I_j is the instrument transfer function in terms of poles and zero, used to correct all seismograms for the instrumental response. The term $2\pi f$ is a factor needed to express the velocity spectral amplitudes.

The displacement source spectrum in the far field approximation is:

$$S_i(f) = \Omega_0 \cdot \frac{f_c^{\gamma}}{f_c^{\gamma} + f^{\gamma}} \qquad (2)$$

where Ω_0 represents the low frequency level depending on the seismic moment (Aki, 1967), f_c is the source corner frequency which is inversely proportional to the source dimension; gamma quantifies the source spectral decay at frequencies higher than f_c. In this study we set the spectral fall-off equal to 2 (see paragraph below).

The attenuation term, quantifying the attenuation along the *ij-th* ray path, is:

$$A_{ij}(f) = exp\ [-\pi t^{*} f^{(1-\alpha)}] \qquad (3)$$

where:

t^{*} is the ratio between travel-times and quality factor Q and depends from the velocity and the attenuation structure of the medium traveled by seismic energy; α quantifies the dependency of quality factor Q from frequency and assumes values from 0 to 1.
In agreement with previous studies (Adams and Abercrombie, 1998; Rietbrock, 2001), for lower magnitude events (higher frequencies) we found a weak to null dependence of Q from the frequency, while for the class of largest magnitudes (ML 4.0-5.0) a dependency of Q from the frequency is observed (see the Figure S1 in the Supplemental Material, and its description for further details).
In this study we chose to set α = 0.0, i.e. consider Q frequency-independent, because the vast majority of the analyzed events belongs to the lower magnitude classes 2-3 and 3-4 (see Table 1): we are

therefore confident that setting $\alpha = 0$ is a licit assumption as already stated in previous studies based on spectral modeling and attenuation tomography (e.g. Boatwright et al., 1991; Rietbrock, 2001; Edwards et al., 2008). Furthermore, the use of frequency-dependent Q (i.e. varying the α values) would imply several attenuation models (e.g. Koulakov et al. 2011), resulting into a complexity which is beyond the scope of this work.

Inserting in equation (1) the terms expressed by (2) and (3), the observed spectrum, corrected for $I_j(f)$, may be expressed as:

$$log_{10}\left[\frac{V_{ij}(f)}{2\pi f}\right] = log_{10}[\Omega_0] + log_{10}\left[\frac{f_c^{\gamma}}{f_c^{\gamma}+f^{\gamma}}\right] - 0.434 \cdot \pi \cdot t^{*}[f^{(1-\alpha)}] \quad (4)$$

We refer to this equation to describe the modeling methodology. Using all the spectral observations for a seismic event, we find a common source corner frequency f_c and, for each single station, the attenuation operator (t*) and low frequency level (Ω_0). This approach has been previously introduced by Stachnik et al., 2004 and applied to P- and S-waves spectra of subduction seismic events.
The estimated values of these unknowns (f_c, t*,Ω_0) for P and S waves spectra, are subsequently used to compute the source parameters assuming the circular crack model of Brune (1970). We compute the seismic moment (M_0), the fault radius (r) and static stress drop ($\Delta\sigma$) by the following relations:

$$M_0 = \frac{4\pi\varrho V_S^3 D\Omega_0}{F R_{\vartheta\phi}} \quad (5)$$

$$r = \frac{Kp,s\,(V_S)}{f_{c\,PS}} \quad (6)$$

$$\Delta\sigma = \frac{7}{16}\frac{M_0}{r^3} \quad (7)$$

Assuming that, in these equations, the same letters have the same physical meaning, as in equation (5), Ω_0 is the low frequency level of the displacement spectrum of the analyzed phases, D is the epicentral distance, ϱ and Vs are the density and S-wave velocity of the medium, respectively. R is the average radiation pattern coefficient equal to 0.52 and 0.62 for P- and S-waves respectively (Boore and Boatwright, 1984), F is the free surface amplification set to 2. In equation (6) Kp,s is a constant

that depends on the adopted circular model and according to the Madariaga model its value is 0.32 and 0.21 for P- and S-waves, respectively (Madariaga, 1976).

To compute the error on stress-drop determinations we account for the errors related to all the variables that enter in equation (7). Thus, the error on the seismic moment (or low frequency level as in equation (5)) and seismic radius (function of fc) are the input for the estimation of stress drop uncertainty that, following Fletcher et al., 1984, may be expressed by:

$$\left(\frac{\sigma_{sd}}{\Delta\sigma}\right)^2 = \left(\frac{\sigma_M}{M_o}\right)^2 + 9\left(\frac{\sigma_r}{r}\right)^2 \qquad (8)$$

where σ_{sd}, σ_M and σ_r are the uncertainties on stress drop, seismic moment and seismic radius, respectively, while $\Delta\sigma$, M_o and r are the corresponding absolute estimates.

Dataset

The Emilia 2012 seismic sequence developed along the compressional system of the Apennines, on the central portion of the Ferrara front (Figure 1).

The sequence was characterized by two main thrust earthquakes (M_L=5.9, 2012-05-20, hh 02:03 UTC; M_L=5.8, 2012-05-29, hh 07:00 UTC) that activated an almost 50 km long fault system elongated in WE direction. Most of the seismicity was located beneath the Po plain alluvial sediments at depths ranging from 5 to 10 km (Chiarabba et al., 2014, Pezzo et al., 2018). After the occurrence of the first mainshock, a dense array of temporary stations was deployed in the epicentral region to follow the spatial and temporal evolution of the seismic sequence. For this study we use a total of 1748 aftershocks as initial data-set, with 22,544 P- and 15,179 S-phases, handily analyzed for accurate estimation of the P- and S-phases onset (Govoni et al., 2014) and used for Vp and Vp/Vs tomography and earthquake locations (Chiarabba et al., 2014; Pezzo et al., 2018) (Figure 1).

The waveforms analyzed in this work are available through the European Integrated Data Archive (EIDA) web-services (https://www.orfeus-eu.org/data/eida/webservices/) (Strollo et al., 2021). We extract P- and S-waves amplitude spectra of seismograms recorded at local distances by velocity seismometers with natural periods of 40s (HH channels, following the convention of EIDA, for Italian archive, see Strollo et al., 2021) and 5s (EH channels), for permanent and temporary stations, respectively (doi:10.13127/SD/X0FXNH7QFY). All waveforms are sampled at 100 Hz.

The records are corrected for instrumental response quantified by poles and zeros of transfer function by using the standard Seismic Analysis Code routines [SAC] (Goldstein and Snoke, 2005; Helffrich et al., 2013). The magnitude (M_L) interval of the events ranges from 1.4 to 5.6.

Since the bandwidth limitation imposed by the waveforms sample rate (100 Hz) limits the estimation of the corner frequency for frequencies above the anti-alias filter corner frequency (40 Hz), we restrict our analysis to earthquakes with magnitude $M_L \geq 2$ (1,306 events). Most of the used aftershocks (1,141) have magnitudes $2 \leq M_L < 3$ while the remnant dataset consists of 151 events in the range $3 \leq M_L < 4$, and 14 with $M_L \geq 4$.

To complete our analysis, we also compute the source parameters of the most energetic events of the sequence, consisting of two mainshocks (M_L=5.9, 2012-05-20, hh 02:03 UTC; M_L=5.8, 2012-05-29, hh 07:00 UTC) and three additional M5+ events (M_L=5.1, 2012-05-20, hh 03:02 UTC; M_L=5.2, 2012-05-20, hh 13:18 UTC; M_L=5.0, 2012-06-03, hh19:20 UTC; see Figure 1). These earthquakes are not included in the bulk of aftershocks but are processed separately using only S-waves spectra for the following motivations: the spectral analysis of a M5+ event requires time windows above 10s due to the low frequency content of the seismic signal; for P-wave spectra analysis, such time windows require a S-P time of at least 10s that is compatible with epicentral distances greater than 45-50 km, i.e. outside the tomographic model (see Pezzo et al., 2018) that we use to locate the aftershocks and to correct the seismic spectra for attenuation; to apply a similar tomographic correction for stations farther than 50 km, a 3D tomographic model at regional scale is required, and although different regional velocity models have been determined for Italy (Di Stefano et al., 2009; Scafidi et al., 2009), no attenuation models have been published so far.

For such events, we use stations deployed in the Alps, north of the epicentral region, and in the northern Apennines, on the south, at distances from 50 to 250 km. For the two mainshocks we use stations at epicentral distance up to 600 km. For these events the attenuation correction of the observed spectra is performed by using the Q estimated from the spectral high frequency decay, as is done for all the analyzed events at the Step-01 of the multi-step procedure described in the next section.

To compute P- and S-wave spectra, we isolated on the vertical (P-wave) and transverse (S-wave) components of seismograms a time window that is a function of the magnitude (Abercrombie, 1995). For the smallest events ($2 \leq M_L < 3$) we use time windows of 1.28s that are increased to 2.56s and 5.12s for events in the magnitude interval 3-4 and 4-5, respectively (see Table 2). For the largest events ($M_L > 5$), we use a time window of 10.24s. For P-waves time windows, in order to prevent contamination by S-waves arrivals, we select only those seismograms where the differential times between S and P phases is greater than the selected P-time window.

After tapering the time window to reduce the effects of limited record lengths, we compute the spectral content by using the FFT. A Hanning window is then used to smooth the resulting spectrum. To evaluate the noise level, we applied the same procedure on a time window of the same length preceding the P-wave signal. We use the same noise window for the P- and S-signals.
The spectral band usable for the analysis begins from the smallest frequency resolvable by the used time length and extends to the antialiasing digitizer filter (40 Hz). For a spectrum to be usable, we search for a continuous long band where the signal to noise ratio is greater than 1.5. This band is chosen depending on the magnitude interval of the events and on the type of computation we are performing (Table 2). The threshold of 1.5 for the signal to noise ratio has been chosen because we are interested in determining the source parameters of smaller earthquakes, and has been applied only to waveforms that have been previously accurately picked (see Govoni et al., 2014). This still permits to retain good-quality spectral amplitudes for robust identification of spectral parameters (examples for a lower magnitude event, $M_L \approx 2$, are pictured in Figure S2 of the Supplemental Material).

Spectral fit for f_c, Ω_0 and t* determination

P- and S-spectra are processed separately by using the same procedure. For a generic seismic event, we use simultaneously all the P or S-wave spectra that meet the S/N selection criteria and we apply a grid-search at 0.1 Hz steps, over the complete frequency range, within the anti-aliasing digitizer filter (40 Hz), computing the event f_c, common to all the stations, and single stations Ω_0 and t* (see Table 2 for the chosen frequency ranges).
For each frequency assumed as trial f_c, we correct the observed spectrum subtracting the second addend of the right side of (4) from the left side of (4). Thus, the corrected spectrum $C_{ij}(f)$ of the station *j-th* is:

$$C_{ij}(f) = log_{10}\left[\frac{V_{ij}(f)}{2\pi f}\right] - log_{10}\left[\frac{f_c^{\gamma}}{f_c^{\gamma}+f^{\gamma}}\right] \quad (9)$$

and equation (4) reduces to:

$$C_{ij}(f) = log_{10}[\Omega_0] - 0.434 \cdot \pi \cdot t^*[f^{(1-\alpha)}] \quad (10)$$

This is the equation of a straight line in the form $C_{ij}(f)$ versus $f^{(1-\alpha)}$ where the slope is $-0.434 \cdot \pi \cdot t^*$ and the intercept is $log_{10}[\Omega_0]$.

We perform for each station *j* a linear regression of $C_{ij}(f)$ as function of $f^{(1-\alpha)}$ to find the unknown parameters of the straight line (Stachnik et al., 2004). From the slope, we estimate the t* along the path *ij-th* while the intercept is used to find the low frequency plateau Ω_0. The goodness of the trial fc is quantified by computing a cost function that accounts for the difference between observed and theoretical spectral amplitudes for all the spectra of the event. Following Edwards et al. (2008) and De Lorenzo et al. (2010), we use as cost function the RMS of amplitudes that in L2 norm is defined as:

$$RMS = \sqrt{\frac{1}{N}\sum_{j=1}^{N} (V_{ij}^{obs} - V_{ij}^{th})^2} \quad (11)$$

where V_{ij}^{obs} and V_{ij}^{th} are the observed and theoretical amplitudes estimated by the computed parameters (the assumed fc, and single station Ω_0 and t*), N is the number of the discrete frequencies over which the summation is computed. All the RMS values computed for each trial fc define the misfit function (MF). The event fc is the frequency for which we observe the minimum of MF.

Method: multi-step procedure

Our procedure consists in resolving the fc – t* trade off with a progressive refinement of parameters from a first fit of velocity spectra for extracting site response at each station from residuals amplitude of spectra fit (Step-01). Then, with the estimated site response, we refine the spectral fit for t* and compute a 3D attenuation tomography (Step-02). Finally, with the theoretical t* computed within the 3D Q model, we refine the computation of fc and source parameters (Step-03). The entire procedure is summarized in the following scheme:

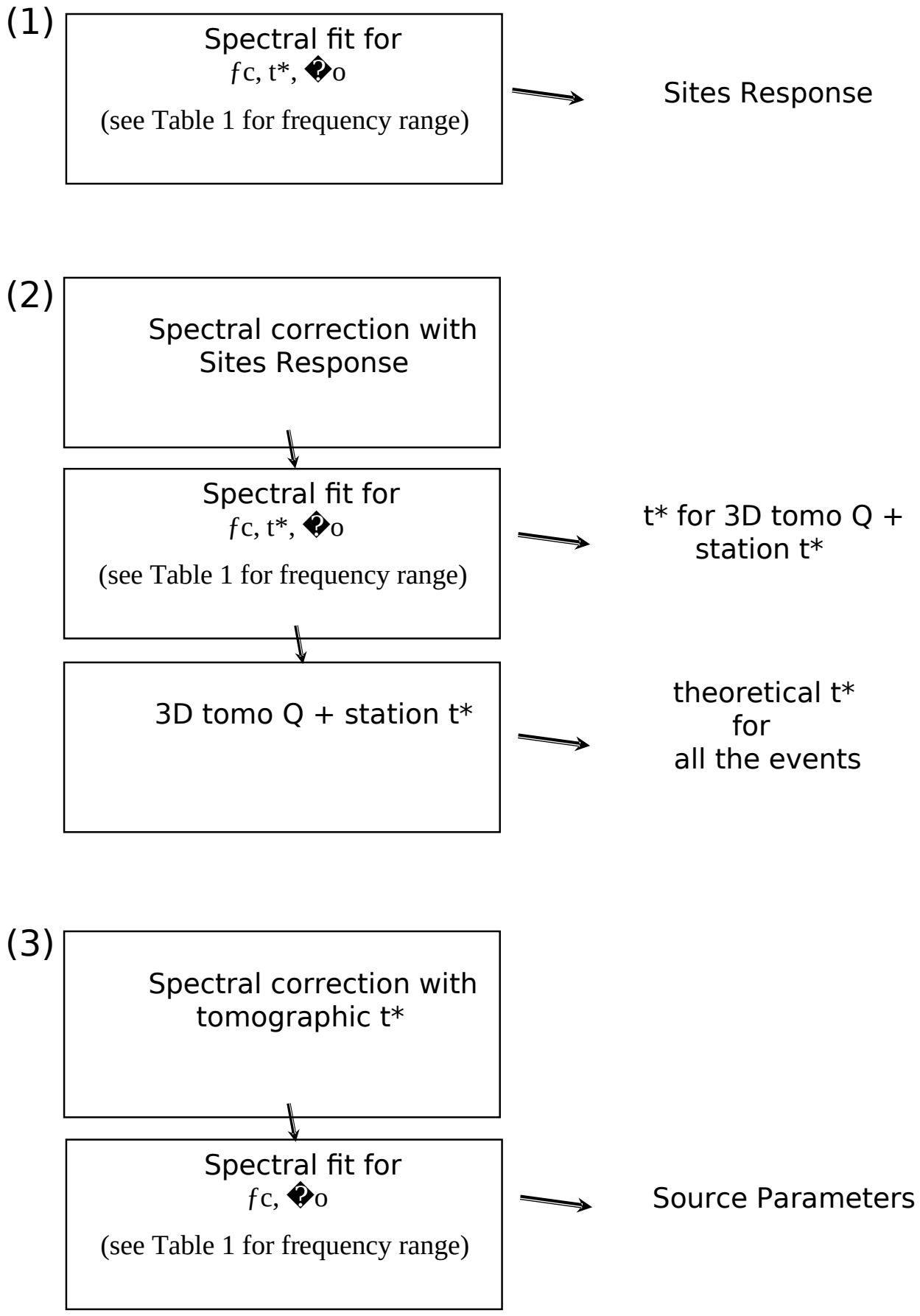
(1)
Spectral fit for
fc, t*, Ωo
(see Table 1 for frequency range)
Sites Response
(2)
Spectral correction with
Sites Response
Spectral fit for
fc, t*, Ωo
(see Table 1 for frequency range)
t* for 3D tomo Q +
station t*
3D tomo Q + station t*
theoretical t*
for
all the events
(3)
Spectral correction with
tomographic t*
Spectral fit for
fc, Ωo
(see Table 1 for frequency range)
Source Parameters

In all the described steps, we fit the spectra by using the grid-search method illustrated above while the frequency band we used depends on the type of computation, as summarized in Table 2.
Examples of the fitting procedure in the three different steps are shown for the P- and S-waves, respectively, in Figures S2, S3, and S4 of the supplemental Material.
The most important aspect of studies focused on the determination of source parameters is related to the estimation of fc and of its errors. We discuss this point in a dedicated section (see below).
We now describe in more detail each step of the adopted procedure.

Method Step-01: computation of site response

We select all the P- and S-waves spectra where the S/N ratio is above the threshold in the complete resolvable frequency band according to Table 2. Then, we compute the event fc and the single station Ωo and t*, with a grid search over the complete frequency band resolvable by the used time window (Table 2).
Once we find the best fit model for each event, we compute the site amplification $R_j(f)$ following the method of Tsumura et al. (1996), Edward et al. (2008) and Edward and Rietbrock (2009). The site response spectrum is expressed by the average of residuals obtained at discrete frequencies considering all the spectra recorded by each station. It is defined by:

$$log_{10}[R_j(f)] = \frac{1}{N} \bullet \sum_{i=1}^{N} \quad log_{10}\left[\frac{V_{ij}^{obs}}{V_{ij}^{th}}\right] \qquad (12)$$

where N is the number of events recorded by the station j-th.
The averaging over a large number of spectra with different azimuthal paths can be considered a proxy of the near site structure beneath each seismic station.

Method Step-02: computation of t* and attenuation tomography

The second step consists in the estimate of t* and the computation of the 3D Q model. In this step, we reselect all the spectra searching for a continuous band where the signal to noise ratio is greater than the threshold within the analyzed frequency band (Table 2). This choice enables to increase the number of spectra usable for tomography without decreasing the quality of the dataset. We use the site correction $R_R(R)$, as computed in Step-01, as a priori information in equation (1) to correct the

observed spectrum for shallow effects. Then we applied the same grid search described above for computing fc and t* values.

The goodness of the final fit is quantified by the RMS, that is also used to assign data weights for the Q inversion (weights of 0, 1, 2, 3 for RMS less than 0.1, 0.2, 0.3, 0.4, respectively, following Eberhart-Phillips and Chadwick, 2002). t* values are discarded if RMS is equal or greater than 0.4 and in the few cases where the t* lead to unrealistic Qp and Qs values (Q > 5,000).

We select a total of 5,021 t* from 526 events and 8,079 t* from 940 events for Qs and Qp inversion, respectively. The inversion of t* for the three-dimensional Qp and Qs structure is based on the following relationship:

$$R* = \int_{RRRRRRR} \frac{RR}{R_{(R)}R_{(R)}} + R^{*}_{RRRR} \qquad (13)$$

where *V(r)* and *Q(r)* are the velocity and the quality factor along the segments of ray with length *dr*. The term t* site accounts for the shallow attenuation beneath the recording site (that may have strong influence on the observed spectrum and differs from the site response $R_R(R)$). Since rays are traced in a known three-dimensional velocity model, t* only depends on the Q structure. Hypocenters located within the three-dimensional velocity model are, at this point, kept fixed and equation (13) is solved, similarly to travel-time tomography, to find the Q structure (see Rietbrock, 2001). The tomographic model is represented by a grid of nodes and the inversion is carried out by an iterative damped least squares approach where Q values are updated at each iteration while velocity values remain fixed to their starting heterogeneous values (Rietbrock, 2001).

Method Step-03: Spectral correction with tomo Q and computation of source parameters

After the determination of the Q models, we compute the synthetic t* by tracing all the seismic rays of our dataset within the 3D velocity and Q model. It is noteworthy that the number of synthetic t* is greater than t* inverted for tomography, as the real data underwent a selection process that diminishes its amount. Hence, at this point of the workflow, all the observed spectra have their correspondent synthetic t* although some of them did not contribute to defining 3D Q structure.

In this final step, for each event, we fit the spectra fixing the attenuation term to that obtained in the 3D Q (Qp or Qs) structure. The spectral modeling is carried out by using the same selection criteria adopted in Step-02 (Table 2). We perform a grid-search to find the optimal fc for P- and S-waves

spectra. For each trial f_c we apply equation (10) keeping t* fixed to the tomographic value and we find the unique unknown represented by the low frequency level Ωo at each station. This approach strongly increases the precision of f_c determination and allows to retrieve many spectra, previously discarded for bad fitting quality (see below).

Step-01: Results (Site Response)

In Figure 2a we show some representative examples of site responses computed by equation (12) for P- and S-waves spectral fit. For a generic seismic station, all the residuals between the observed and theoretical amplitude are averaged at each frequency, thus reducing the effect related to the source and outlining the contribution of the shallow structure beneath the recording site. While below 10 Hz the site responses do not show large variations and the trends are almost confined around 1.0 Hz, at higher frequencies (>10 Hz) we observe larger fluctuations with peaks between 10-20 Hz. Assuming a mean velocity of 3 km/s and 1.6 km/s for P- and S-waves at shallow depths (Chiarabba et al., 2014; Pezzo et al., 2018), these frequencies are compatible with wavelengths of a few hundred meters. Therefore, the observed large amplification effects are related to small scale complexities located at very shallow depths beneath the recording sites. Although the detailed interpretation of site responses is beyond the scope of this paper, we try to explain these observations. If we correlate the mean amplitude of site response observed between 10 and 20 Hz with station residuals obtained by travel time tomography by Pezzo et al. 2018 (Figure 2b) we observe that, while P-station residuals do not show any apparent correlation with site responses, S-station residuals exhibit a weak positive correlation. This evidence suggests that the 10-20 Hz peaks of site response are related to shallow volumes where S-waves are slowed, probably due to the thicker soil coverage. It is important to remark that site responses act as a site transfer function in Step-02 and Step-03 of workflow. The use of site correction improves the spectral fit of P- and S-wave spectra, decreasing the final RMS of about 10% with respect to a starting fit without the application of the site response correction.

Step-02: Results (tomo Q)

For the tomographic inversion we use the results of spectral fit of Step-02. We select only those events with at least 4 usable t*, resulting in a total of 5,021 t* (from 526 events) and 8,079 t* (from 940 events) for Qs and Qp inversion, respectively. For both earthquake locations and grid spacing we

mirror the tomographic model of Pezzo et al. (2018) that acts, in this study, as a priori information. We use nodes spaced 5 km in horizontal directions and 3 km along depth. For each node, we assign a starting value for Qp and Qs in addition to the 3D velocity estimates (Vp, Vs) derived from the tomographic model of Pezzo et al. (2018).

The uniform initial Qp and Qs value is selected by a grid-search approach. We minimize the RMS of residuals computed with the observed t* and the synthetic ones that we obtain by tracing all seismic rays through the model where 3D velocity distribution and trial uniform Q values are defined (Rietbrock, 2001). The minimization of RMS leads to a uniform Qp and Qs value of 300 as starting values for tomography. We select the optimal damping for the inversion according to the trade-off curves between model complexity and data misfit (see Figure 3a).

For 3D inversions, Qp and Qs adjustments are computed only for nodes intersected by more than 10 rays. After 5 iterations, the final RMS is 0.005 (Variance Improvement around 49 %) and 0.007 (Variance Improvement of 80%) for Qp and Qs inversion, respectively.

The model resolution is quantified by computing the Spread Function (SF, Michelini and McEvilly, 1993). Following the method of Toomey and Foulger (1989), we select SF=3 as a reliable threshold below which Qp and Qs nodes are characterized by a satisfactory ray sampling and compact averaging vector (i.e., vectors picked on their diagonal values).

Again, since a detailed interpretation of the 3D attenuation tomography results is beyond the scope of this paper, we limit our description to the main features at significant depths (Figure 3b). Both Qp and Qs models show nearly checkerboard patterns of relatively high (lower attenuation, blue areas) and low values (higher attenuation, red areas) at shallow depths (0-3 km), reflecting the complexity of the attenuation structure in the sedimentary cover and at very local scale. At intermediate depths (around 6 km) the attenuation pattern shows a prevalence of higher values (Qs up to 400, lower absorption) in the central part of the Qs model, while the Qp structure is more complex, with a prevalence of relatively high attenuation (Qp down to 200) in its central part. It is noteworthy that the bulk of earthquakes at this depth (including the first mainshock, yellow star in Figure 3b) occur at the boundary between relatively higher and lower attenuation volumes, both in the Qp and in the Qs models. Finally, at greater depths (around 9 km), a broad relatively low attenuation characterizes both the Qp and Qs models. Here high Qp and Qs (both up to 400) volumes contain the seismicity, including the second mainshock (purple star in Figure 3b).

Step-03: Results (Source Parameters)

At the end of Step-03 of workflow all the usable spectra are corrected for attenuation by means of 3D attenuation tomography. For each event, we estimate a common source corner frequency and single stations low frequency levels. Based on the quality of spectral fitting (Eberhart-Phillips and Chadwick, 2002), we retain all the events with at least 4 spectra with fit-quality of 0, 1, 2, discarding the worst fit with weight > 2. This selection criterion reduces the number of available events for source parameter computation but provides the best fit for robust computations of source parameters.

We now consider the application of classical equations (5), (6) and (7) for the computations of the static source parameters. Errors on source parameter estimation are discussed in the next section. From the event source corner frequency, we compute the source dimension (r) by applying equation (6). Since we have one value of fc for each event, the seismic radius is not averaged among the stations of the events but it is simply a single value. The estimation of the event seismic moment is performed averaging the contribution of each station. For each estimate of the low frequency level (Ωo), we apply equation (5) by using Vs= 3.5 km/s, as average velocity of the seismic volume (Pezzo et al., 2018) and a crustal density of 2800 kg/m^3. For the geometrical spreading that enters in equation (5), since our dataset consists of earthquakes recorded at short epicentral distance, the simple 1/D function is a valid assumption (Edward et al., 2008; De Lorenzo et al., 2012). From the estimation of seismic moment, we compute the moment magnitude (Mw) through the relationship (Hanks and Kanamori, 1979):

$$M_w = \frac{2(log\ Mo - 9.1)}{3} \qquad (14)$$

where Mo is the seismic moment expressed in Nm.
Mo and source dimensions are subsequently used in equation (7) to calculate the released stress drop.

In Figure 4, we present the results of the static source parameters obtained by the P- and S-wave spectra (from 1207 and 1171 events, respectively) by 3 different bi-dimensional plots. We show the variation of seismic moment versus the source dimension (Figure 4, top panel) and released stress drop (Figure 4, middle panel), In addition we report the distribution of the source corner frequency against the Moment magnitude (bottom panel in Figure 4). On the first and last plot, we superimpose the black lines that delineate the values of constant stress drop. All the aftershocks processed by the described procedure are represented in Figure 4 by circles with size and color depending on the magnitude (according to the legend on the bottom panels). Stars are the events with magnitude greater than 5, including the two mainshocks, that we have treated separately, without the use of Q

tomography, that are included to realize a complete analysis of the source parameters of the study sequence. At the end of our multi-step procedure we obtain the estimates of the static source parameters for a total of 1240 aftershocks.

As a general observation, we note that source parameters computed by using P- and S-wave spectra give similar results. Our data show that Seismic Moments span over about 5 orders of magnitude, from 10^{11} Nm to 10^{16} Nm, while seismic radii are in the range 30-650 m. The seismic moment and the source dimension show approximately a linear trend. Although points are bound by lines of constant stress drop that cover 2 orders of magnitudes, these observations are compatible with the earthquake scaling of constant stress drop, as widely reported in many studies worldwide (see Abercrombie, 2021). In our case, stress drops of aftershocks are mostly confined between 1 and 100 Mpa. The log-space mean value of the aftershock stress drop is displayed by histograms of Figure 5a. P- and S-waves analysis gives similar results: the average stress drop is of about 6.7 Mpa for P- and S-waves, with a ratio of 1.07. The largest events, with stress drop ranging from 1 to 10 Mpa, are in agreement with the aftershocks averaging values and exhibit source dimensions coherent with a linear trend (Figure 4, top and bottom panels).

The corner frequencies are mostly in the range 3-30 Hz and 2-25 Hz for P-and S-waves, respectively (Figure 4, top and bottom panels). The ratio between f_cP and f_cS, estimated from the log-normal histogram, is 1.70 (see Figure 5b). Since the log-space standard deviation is 0.09, the confidence limits of mean ratio are between 1.37 to 2.10, which is a variability that includes the theoretical estimates of 1.5 based on the circular rupture model (Madariaga, 1976).

We also compare the moment magnitude Mw determined with P- and S-spectra with the local magnitude determined by the INGV analysts (Iside Working Group, 2007). Even if for M_L smaller than about 2.5-3.0 we observe a larger scatter of data, the scatter plot of the Mw versus M_L is fairly well represented by a 1:1 relation for all the magnitude range, both for P- and S-waves data (Figure 6).

We fit our M_L-Mw data by an orthogonal regression that minimizes the Euclidean the distance between each data point and the fitting line (Golub and van Loan, 1980). This approach should be preferred to the standard regression strategies when data are affected by unknown uncertainties (in our pool of data this is the case of M_L, see Di Bona, 2016). To compute the error on the slope and the intercept, we apply the bootstrap method with 1000 resamples of the original data distribution computing a regression for each realization (Figure 6). For each fitting line, the slope and its error, as well as the intercept and its standard error, are reported in Figure 6.

The self-similarity of earthquakes

Earthquakes are defined as self-similar when the released stress-drop is constant. This means that the event magnitude and the surface rupture increase or decrease according to equation (7). From equation (7), taking the logarithms, we can write:

$$log10\,(\,Mo) = log10\,(2.2857\,\Delta\sigma) + 3\,log10\,(r) \qquad (15)$$

Reporting in a two-dimensional plot the seismic moment as a function of the fault dimension (as in the top panels of Figure 4) for the analyzed dataset, if the self-similar trend is respected, the events should define a straight line with slope equal to 3 and an intercept that is function of the constant stress drop value.

To verify if our dataset is in agreement with the self similar model, we fit the P and S waves dataset with a free straight line (dashed lines in top panels of Figure 4) and with equation 8 where the slope is fixed to 3. The corrected Akaike criterion is applied in order to understand whether the constant stress drop model is better, in a statistical sense, than the case where stress drop increases with source dimensions. For P-wave data (Figure 4 left), the modified Akaike criterion indicates that fitting line with slope fixed to 3 is significantly better, in a statistical sense, than the free straight-line, suggesting a self-similar behavior. For S-wave data (Figure 4 right) the same statistical test strongly supports the fitting line whose slope is greater than 3 (slope=3.443), suggesting that stress drop is proportional to source dimension, therefore violating the self-similarity concept.

The breakdown of earthquake self-similar scaling, as seen through S-waves analysis, has been observed in quite a few studies on single seismic sequences (e.g., Pacor et al., 2016; Wang et al., 2019, and references therein). In our case, the fact that P-wave data shows a self-similar behavior differently to what the S-waves suggest, leads to an apparent incongruence that deserves further specific studies.

Error analysis on source parameter estimation

The crucial point for studies focused on the determination of source parameters is the estimation of fc and its uncertainties. Stress drop, in fact, is proportional to the cubes of fc (see equation (6) and

(7)) and the error on fc propagates heavily on the uncertainty of stress drop (see equations (6),(7), and (8)).

For example, assuming an S-wave spectrum characterized by a low frequency level Ωo of 1e-6 and fc=10 Hz with 1Hz of standard deviation (relative error of 10%), the stress drop value ranges approximately from 10 to 18 Mpa if other sources of errors are neglected. If the standard deviation is of 2 Hz (relative error of 20%), stress drop could vary between 7 and 24 Mpa. The same calculation carried out at fc=20 Hz gives larger stress drop variations with values from 80 to 150 Mpa.
A wide variability of stress drop error is reported in literature. For example, Cotton et al. (2013) states that the approaches that rely on spectral determination of seismic moment and corner frequencies lead to large scatter in stress drop determination and to large uncertainties in predicting seismic hazard. In our case we are confident that correcting spectra for tomo Q give reliable fc determination and robust stress drop determinations.

For each event, and for each step of our procedure, we compute accurately the error on fc by using two independent approaches. When both methods provide similar error estimates, we are confident that the fitting approach is giving robust results and the final fit is retained. Conversely, when the two methods give different estimation of fc error, the final fit is discarded.
First, we quickly estimate the fc uncertainty by means of the second derivative of the Misfit Function (MF) curve around its minimum (Menke, 2018). It follows that the fc error is strongly dependent on the shape of the misfit function (MF). When the MF curve is characterized by a well picked minimum, the fc error is small, conversely an almost flat MF leads to ambiguous fc and to large error estimates.
To strengthen the evaluation of errors about fc (for P- and S-waves spectra), we furtherly applied, for each event, a method based on a bootstrap approach, described in YEA for coda spectra. Once the event fc and single stations Ω_0 and t* have been defined by MF analysis, we computed the residuals between observed and theoretical amplitudes. To create a bootstrap sample, we randomly take values from residuals dataset allowing the selection of a single value more than once. This is the "replacement" process of bootstrap statistics (Efron, 1979). The resampled values are then summed to the theoretical amplitudes to obtain the simulated spectra of the event. These spectra are then fitted as in the real case to find the event fc and single stations Ω_0 and t*. For each event, we perform 1,000 bootstrap realizations, thus collecting 1,000 values of fc from which we construct a histogram that describes the sampling distribution from which we compute the mean fc and its standard error. The fc characteristics (mean, and standard deviation) bootstrap-derived are then compared with those derived by the MF curve. When both methods provide similar fc and related error estimates, we are confident that spectral fits are robust and the subsequent estimation of source parameters are reliable. Conversely, a disagreement between MF and bootstrap resampling outcomes suggest that the final fit

is poorly constrained and it should be discarded. After a visual inspection of results, we decided that, for an event to be retained, the maximum threshold between MF and bootstrap results should be within 1.5 Hz.

In Figures 7 and 8 we show, for representative small magnitude event (in the range 2-3), the MF curve and the histogram of the bootstrap resampling for P- and S-waves spectral fitting, respectively, in the first and last part of the workflow (Step-01 and Step-03, see Table 2). At the beginning of Step-01, spectral fit are carried out with any a-priori information while in Step-03 we correct site effects with the site responses obtained at the end of Step-01 and path attenuation with the tomographic t* determined at the end of Step-02.

Small magnitude events (in the range 2-3 M_L), are in general the most problematic in determining a reliable value of f_c (Klinger and Werner, 2022; Parolai and A. Oth, 2022). For the event of M_L=2.2 (Figure 7 and 8 for P- and S-waves fit, respectively), in Step-01, the RMS vs the trial f_c, after an evident decrease of RMS at very low f_c values, show an almost flat trend at increasing f_c, describing an L shaped curve. From a numerical point of view, the minimum exists but it is weak and it is visible only by zooming around the minimum itself (see gray insets in Figures 7 and 8). This observation holds for P- and S-waves fitting run the Step-01 of the workflow.

This trend is mainly due to attenuation effects that mask the source decay and the minimum of the curve is unclear and ambiguous. Consistently, the f_c distribution bootstrap-derived is characterized by an irregular shape with a mean value and a standard deviation very distant from the value obtained by the MF curve (Figures 7a and 8a, for P- and S-spectral fit, respectively). The disagreement between MF and bootstrap derived estimations is the proof that the spectral fit is unconstrained. In this case we skip the P- and the S-spectral fit and this event (M_L=2.2 in Figures 7 and 8) does not contribute to the estimation of site response and of attenuation seismic tomography. After the visualization of results, we decided that the maximum permissible deviation between MF and bootstrap derived estimation (of f_c and standard error) is 1.5 Hz. Above this threshold the spectral fit is discarded.

The main important aspect is that, when the same event is processed by using site response and t* fixed as a priori information, the attenuation effect is decoupled from the source spectral decay and the search for the event corner frequency is strongly improved (Figures 7b and 8b, for P- and S-spectral fit, respectively).

As it is clearly observable in Figures 7b and 8b, the RMS vs f_c is now picked on a well-defined minimum. The bootstrap derived distribution shows that the mean f_c and its standard deviation are almost identical to the values extracted by the MF curve.

This coherence allows us to select the event, previously discarded, for P- and S-source parameter computation. In this range of magnitude (2-3), the introduction of synthetic t* lead to well constrained fit with a remarkable increase of the number of spectra usable for source parameter estimation (see

numbers enclosed in parentheses in Table 1). For S waves, the number of events increases by about 50 % with respect to the events used for tomography. For P waves, this increment is even greater since fewer events are input for tomographic inversion.

At greater magnitudes (classes M_L=3-4 and M_L=4-5) the improvement generated by the tomography is less pronounced, being the number of events almost similar at each step of the workflow (see the Supplemental Material for the description of the MF curves and the histograms for events of greater magnitudes classes). For M_L>3, in fact, the MF curve and bootstrap derived distribution are well defined at each step. The corner frequency is well constrained by a well-defined minimum and the estimated errors are similar (see Figures S5-S6 and Figures S7-S8 of the Supplemental Material for events of M_L 3.9 and M_L 4.4, respectively). We stress that by using Q tomography to correct spectra, the final fit is sensibly improved since the minimum of MF curve is found for RMS values lower with respect to the starting fit.

In addition to the fc, the uncertainties of the other source parameters are computed as follows. At the end of Step-03 of workflow all the usable spectra are corrected for attenuation by means of 3D attenuation tomography. For each event, we estimate a common source corner frequency and single stations low frequency levels. From the source corner frequency, we compute the source dimension (r) by applying equation (6); its error, σ_r, is related to the error on fc estimate (σ_{Fc}) by the relation:

$$\frac{\sigma_r}{r} = \frac{\sigma_{Fc}}{Fc} \qquad (16)$$

For the estimation of the seismic moment, we average the contribution of all the available stations. Since the fitting procedure furnishes the low frequency level and the RMS for each spectrum, we apply equation (5) for each station and we compute the mean seismic moment and its uncertainty under the assumption that data are lognormally distributed (Archuleta et al., 1982; Fletcher et al., 1984). In particular we apply a weighted mean in log space where the fit RMS acts as the inverse of the weight for the station seismic moment. The standard deviation of the mean, that represents the error bar in the logarithmic plot related to the seismic moment, is then converted into the multiplicative factor defined by Fletcher et al. (1984) that enters in equation (8) for the estimation of stress drop error. In this work, the multiplicative factors are in the interval ranging from 0.04 to 0.97 for both P- and S-spectra, a range of values coherent with those reported in Table 2 of Fletcher et al. (1984).

The released stress drop and its error are computed by applying equation (7) and (8), respectively.

In Figure 9 we show the relative uncertainty of stress drop for P- and S-waves compared to the same estimation obtainable in Step-01 and Step-02 of the workflow, without correcting spectra for tomographic attenuation. About 80% of stress drop estimations are characterized by relative error

within 20% with maximum values of about 40% (Figure 9 right-upper and -lower panels, for P and S-spectral fit, respectively). It is worth noting that without the contribution of Q tomography (Step-01 and -02 of the workflow) the number of acceptable fits is sensibly lower and the error quality on stress drop estimation decreases for both P- and S-spectral fit (Figure 9 middle and left panels, for Sept-02 and Step-01, respectively).

Kane et al., (2011), using a frequency domain EGF approach, estimated that the minimum error related to stress drop estimation should be of about 30%. In our approach, at Step-02 of the workflow, for the 80% of events, errors are mostly between 20 and 30% with a few percent of events with error between 30 and 40% (Figure 9 middle-upper and -lower panels, for P and S-spectral fit, respectively). Our results are, on average, coherent with the conclusion of Kane et al. (2011). The spectral correction by using Q-tomography, however, leads to an improvement (Figure 9 right-upper and -lower panels, for P- and S-spectral fit, respectively). For the common events processed in the three steps of the workflow (299 events for P- and 837 for S-waves), we observe that the final reduction of the stress drop uncertainty is, on average, of 48% and 32 % for P- and S-spectral fit, respectively.

Since errors on stress drop are dominated by uncertainty of fc, we are confident that our results benefit from the small error on fc determination.

Comparison of Stress-Drop estimations by direct S– and coda–waves fit

To better assess the performance of our method and to critically evaluate the results, we compare our S-wave fc estimations with those derived by applying the method of YEA, where coda wave spectral ratios are used. We focus our comparison with the YEA method since the estimation of fc relies on seismic waves (coda waves) independent from the S-body waves used in the spectral inversion scheme proposed. The methodology used for this comparison is fully described in the Supplemental Material. For sake of brevity here we only show the results of the comparison between the two approaches. In Figure 10, stress drop values determined through the YEA method are compared with stress drop estimated by the spectral fit procedure. We observe that the points lay on the proximity of the equal-values line (gray line in Figure 10a), showing a substantial agreement between the stress drop values determined by the two independent methods, as matter of fact, the computed linear regression of the data points (red dashed lines in Figure 10a) is characterized by a slope being very close to 1.

If we compare the stress drop variations computed with respect to the average value for the same pool of data, we observe that the majority of points fall in the NE-SW quadrants, delineating a positive correlation between stress drop variations. Since the average stress drop value is determined separately for coda and spectral fit data, this plot demonstrates that both stress drop datasets give equivalent indications about the variability of stress drop with respect to the mean value (Figure 10b)

Conclusions

We computed the source parameters for 1240 aftershocks of the 2012 Emilia sequence (1207 from P-waves and 1171 from S-waves, respectively; 1138 events have estimates from both P- an S-waves), with magnitude ranging from 2.0 to 4.7, by applying two independent methods. First, we use a classical approach based on the spectral fit of P- and S-waves body waves to a data-set of 1,306 seismic events with $M_L \geq 2$. We corrected the attenuation by means of a 3D Qp and Qs tomographic model computed by using the same dataset starting from tomographic models (Vp, Vs) and 3D locations used as a priori information. The results deriving either from P- and S-wave spectral fit are coherent and give similar estimates of source parameters. Seismic moments are in the range 10^{11} - 10^{16} Nm, stress drops values range from 0.1 to 83 Mpa, while the variability of source dimensions is in the interval 30-650 m. P-wave spectral fit gives seismic moment and source dimensions that scale in a self-similar model with an almost constant stress drop of 6.7 Mpa. Conversely, for S waves we obtain a proportionality between stress drop and source dimension suggesting a violation of self-similarity, as observed for other seismic sequences (e.g., Malagnini et al., 2008; Pacor et al., 2016; Wang et al., 2019, and references therein). The fit of Seismic Moment versus f_c shows that $M_o \propto f_c^{-0.3443}$.

Separately, we compute the source parameter following the procedure described in YEA based on the modeling of coda spectral ratio. Our results show that the stress drop estimates are almost similar to that obtained for S-waves spectral fit. This agreement suggests that the assumptions that we choose to perform spectral fit, not required by coda spectral ratio modeling, are in general correct.

Although the method of YEA could lead to high precision stress drop determination for very populated clusters, the analysis conducted by spectral fit by using attenuation tomography gives the opportunity to compute stress drop for a larger number of events, exploiting, for example, entire aftershock sequences. Since the aftershocks, spreading over the main rupture planes and secondary structures, reveal the geometric details of the activated faults (Valoroso et al., 2012; Chiaraluce et al.,

2017), this approach gives the opportunity to analyze the spatial patterns of stress drop variations, hence infer the mechanical state over the whole ruptured fault system.

DATA AND RESOURCES

The seismograms analyzed in this work are available through the European Integrated Data Archive (EIDA) web-services (https://www.orfeus-eu.org/data/eida/webservices/).

The supplemental material contains additional details on the dependency of the quality factor (Q) from the frequency, on the error analysis on source parameter estimation, and on the comparison of Stress-Drop estimations by direct S– and coda–waves fit. Furthermore, it contains examples of spectral fit for lower magnitude events and of the fitting procedure in the different steps of the workflow described in the manuscript.

DECLARATION OF COMPETING INTERESTS

The authors declare that there are no conflicts of interest.

ACKNOWLEDGMENTS

We are indebted to the Associate Editor, Stefano Parolai, and to two anonymous reviewers for their keen reviews; their extremely constructive comments lead to substantial improvements of the original manuscript. We thank Simone Mancini for useful discussion in the early stage of this work.

References

Abercrombie, R. E. (1995). Earthquake source scaling relationships from - 1 to 5 M L using seismograms recorded at 2.5 km depth, J. Geophys. Res. 100, 24015-24036.

Abercrombie R. E. (2021). Resolution and uncertainties in estimates of earthquake stress drop and energy release, Phil. Trans. Roy. Soc. Lond. A 379, no. 2196, doi: https://doi.org/10.1098/rsta.2020.0131.

Adams, D. A., and R. E. Abercrombie (1998). Seismic attenuation above 10 Hz in southern California from coda waves recorded in the Cajon Pass borehole, J. Geophys. Res. 103, 24,257–24,270.

Aki, K. (1967). Scaling law of seismic spectrum, J. Geophys. Res. 72, 1217–1231.

Allmann, B. P., and P. M. Shearer (2007). Spatial and temporal stress-drop variations in small earthquakes near Parkfield, California, J. Geophys. Res. 112, no. B04305, doi 10.1029/2006JB004395.

Bindi, D., R. R. Castro, G. Franceschina, L. Luzi, and F. Pacor (2004). The 1997–1998 Umbria-Marche sequence (central Italy): Source, path, and site effects estimated from strong motion data recorded in the epicentral area, J. Geophys. Res. 109, B04312.

Boatwright, J., J. B. Fletcher, and T. E. Fumal (1991). A general inversion scheme for source, site and propagation characteristics using multiply recorded sets of moderate-sized earthquakes, Bull. Seismol. Soc. Am. 81, 1754–1782.

Boore, D. M. (1983). Stochastic simulation of high-frequency ground motions based on seismological models of the radiated spectra, Bull. Seismol. Soc. Am. 73, 1865–1894.

Brune, J. N. (1970). Tectonic stress and the spectra of seismic shear waves from earthquakes, J. Geophys. Res. 75, 4997–5009.

Chiaraluce, L., R. Di Stefano, E. Tinti, L. Scognamiglio, M. Michele, E. Casarotti, M. Cattaneo, P. De Gori, C. Chiarabba, G. Monachesi, et al. (2017). The 2016 central Italy seismic sequence: A first look at the mainshocks, aftershocks, and source models, Seismol. Res. Lett. 88, no. 3, 757–771, doi: 10.1785/0220160221.

Chiarabba, C., P. De Gori, L. Improta, F.P. Lucente, M. Moretti, A. Govoni, and A.Nardi (2014). Frontal compression along the Apennines thrust system: The Emilia 2012 example from seismicity to crustal structure. Journal of Geodynamics, 82, 98–109, doi: https://doi.org/10.1016/j.jog.2014.09.003.

Cotton, F., R. Archuleta, and M. Causse (2013). What is sigma of the stress drop? Seismol. Res. Lett. 84, no. 1, 42–48.

de Lorenzo, S., A. Zollo, and G. Zito (2010). Source, attenuation, and site parameters of the 1997 Umbria-Marche seismic sequence from the inversion of P wave spectra: A comparison between constant Q(P) and frequency-dependent Q(P) models, J. Geophys. Res. Solid Earth 115, 23 pp.

Di Bona, M. (2016). A Local Magnitude Scale for Crustal Earthquakes in Italy, Bulletin of the Seismological Society of America, Vol. 106, No. 1, pp. 242–258, February 2016, doi: 10.1785/0120150155

Di Stefano, R., E. Kissling, C. Chiarabba, A. Amato, and D. Giardini (2009). Shallow subduction beneath Italy: Three-dimensional images of the Adriatic-European-Tyrrhenian lithosphere system based on high-quality P wave arrival times, J. Geophys. Res., 114, B05305, doi:10.1029/2008JB005641.

Eberhart-Phillips, D., and M. Chadwick (2002). Three-dimensional attenuation model of the shallow Hikurangi subduction zone in the Raukumara Peninsula, New Zealand, J. Geophys. Res. 107, no. B2 (ESE3), 1–15.

Edwards, B., A. Rietbrock, J. J. Bommer, and B. Baptie (2008). The acquisition of source, path, and site effects from microearthquake recordings using Q tomography: Application to the United Kingdom, Bull. Seismol. Soc. Am. 98, 1915–1935.

Edwards, B., and A. Rietbrock (2009). A comparative study on attenuation and source-scaling relations in the Kanto, Tokai, and Chubu Regions of Japan, using data from Hi-Net and Kik-Net, Bull. Seismol. Soc. Am. 99, doi 10.1785/0120080292.

Efron, B. (1979). Bootstrap Methods: Another Look at the Jackknife, Ann. Statist. 7 (1) 1 - 26, doi: https://doi.org/10.1214/aos/1176344552.

Eshelby, J. D. (1957). The determination of the elastic field of an ellipsoidal inclusion and related problems. Proc. Roy. Soc. London Series A, 241, 376–396.

Fletcher, J., J. Boatwright, L. Haar, T. Hanks, and A. McGarr (1984). Source parameters for aftershocks of the Oroville, California, earthquake, Bull. Seism. Soc. Am. 74, 1101–1123.

Goertz- Allmann, B. P., A. Goertz, and S. Wiemer (2011). Stress drop variations of induced earthquakes at the Basel geothermal site, Geophys. Res. Lett., 38, L09308, doi:10.1029/2011GL047498.

Goldstein, P., and A. Snoke (2005). SAC availability for the IRIS community, Incorporated Institutions for Seismology Data Management Center Electronic Newsletter, available at https://ds.iris.edu/ds/newsletter/vol7/no1/193/sac-availability-for-the-iris-community/

Golub, G.H., and C.F. Van Loan (1980). An analysis of the total least squares problem. Numerical Analysis, Vol. 17, pp. 883-893.

Govoni, A., A. Marchetti, P. De Gori, M. Di Bona, F. P. Lucente, L. Improta, C. Chiarabba, A. Nardi, L. Margheriti, N. P. Agostinetti, et al. (2014). The 2012 Emilia seismic sequence (northern Italy): Imaging the thrust fault system by accurate aftershock location, Tectonophysics 622, 44–55, doi: 10.1016/j.tecto.2014.02.013.

Kanamori, H., and D. Anderson (1975). Theoretical basis of some empirical relations in seismology, Bull. Seismol. Soc. Am. 65, 1073–1096.

Kane, D. L., G. A. Prieto, F. L. Vernon, and P. M. Shearer (2011). Quantifying seismic source parameter uncertainties, Bull. Seismol. Soc. Am. 101, 535–543, doi: 10.1785/0120100166.

Koulakov, I., Bindi, D., Parolai, S., Grosser, H., and C. Milkereit (2010), Distribution of Seismic Velocities and Attenuation in the Crust beneath the North Anatolian Fault (Turkey) from Local Earthquake Tomography, Bulletin of the Seismological Society of America, Vol. 100, No. 1, pp. 207–224, February 2010, doi: 10.1785/0120090105

Klinger, A. G., and M. J. Werner (2022). Stress drops of hydraulic fracturing induced microseismicity in the Horn River basin: Challenges at high frequencies recorded by borehole geophones, Geophys. J. Int. 228, no. 3, 2018–2037, doi: 10.1093/gji/ggab458.

Ko, Y., B. Kuo, and S. Hung (2012). Robust determination of earthquake source parameters and mantle attenuation, J. Geophys. Res. 117, no. B4, doi: 10.1029/2011jb008759.

Hanks, T. C., and H. Kanamori (1979). A moment magnitude scale, J. Geophys. Res. 84, no. B5, 2348–2350.

Helffrich, G., J. Wookey, and I. Bastow (2013). The Seismic Analysis Code: A Primer and User's Guide, Cambridge University Press, New York, New York.

Herraiz, M., and F. Espinosa (1987). Coda waves: A review, Pure Appl. Geophys. 125, 500–577.

Hough, S. E. (1997). Empirical Green's function analysis: taking the next step, J. Geophys. Res. 102, 5369–5384.

Hough S. E. (2001). Empirical Green's function analysis of recent moderate events in California, *Bull. Seismol. Soc. Am.* 91, 456–467.

Ide, S., G. Beroza, S. Prejean, and W. Ellsworth (2003). Apparent break in earthquake scaling because of path and site effects on deep borehole recordings, J. Geophys. Res. 108, 2271, doi 10.1029/2001JB001617

Imanishi, K., and W. L. Ellsworth (2006). Source scaling relationships of microearthquakes at Parkfield, CA, determined using the SAFOD Pilot Hole seismic array, in Earthquakes: Radiated Energy and the Physics of Faulting, R. E. Abercrombie, A. McGarr, H. Kanamori, and G. Di Toro (Editors), American Geophysical Monograph 170, 81–90.

ISIDe Working Group. (2007). Italian Seismological Instrumental and parametric Database (ISIDe). Istituto Nazionale di Geofisica e Vulcanologia (INGV). https://doi.org/10.13127/ISIDE

Lees, J. M., and G. T. Lindley (1994). Three-dimensional attenuation tomography at Loma Prieta: Inversion of t* for Q, J. Geophys. Res. 99, 6843–6863.

Madariaga, R. (1976). Dynamics of an expanding circular fault, Bull. Seism. Soc. Am. 66, 639–666.

Malagnini, L., L. Scognamiglio, A. Mercuri, A. Akinci, and K. Mayeda (2008). Strong evidence for non-similar earthquake source scaling in central Italy, Geophys. Res. Lett. 35, L17303, doi: 10.1029/2008GL034310.

Mayeda, K., and W. R. Walter (1996). Moment, energy, stress drop, and source spectra of western United States earthquakes from regional coda envelopes, J. Geophys. Res. 101, 11,195–11,208.

Mayeda, K., L. Malagnini, and W. R. Walter (2007). A new spectral ratio method using narrow band coda envelopes: Evidence for non-selfsimilarity in the Hector Mine sequence, Geophys. Res. Lett. 34, L11303, doi 10.1029/2007GL030041.

Menke, W. (2018). Geophysical Data Analysis: Discrete Inverse Theory, Academic Press, San Diego, California.

Michelini, A., and T. V. McEvilly (1991). Seismological studies at Parkfield, part I: Simultaneous inversion for velocity structure and hypocenters using cubic B-splines parameterization, Bull. Seism. Soc. Am. 81, 524–552.

Moretti, M., L. Abruzzese, N. Abu Zeid, P. Augliera, R. Azzara, L. Benedetti, A. Bono, P. Bordoni, T. Boxberger, and A. Bucci et al. (2012). Rapid response to the earthquake emergency of May 2012 in the Po Plain, northern Italy, in 2012 Pianura Padano-Emiliana Seismic Sequence, special issue, Ann. Geophys. 55, no. 4, doi: 10.4401/ag-6152.

Oth, A., D. Bindi, S. Parolai, and F. Wenzel (2008). S-wave attenuation characteristics beneath the Vrancea region in Romania: New insights from the inversion of ground-motion spectra, Bull. Seismol. Soc. Am. 98, 2482–2497.

Oth, A., D. Bindi, S. Parolai, and D. D. Giacomo (2011). Spectral analysis of K-NET and KiK-net data in Japan, Part II: On attenuation characteristics, source spectra, and site response of borehole and surface stations, Bull. Seismol. Soc. Am. 101, 667–687.

Pacor, F., D. Spallarossa, A. Oth, L. Luzi, R. Puglia, L. Cantore, A. Mercuri, M. D'Amico, and D. Bindi (2016). Spectral models for ground motion prediction in the L'Aquila region (central Italy): Evidence for stress-drop dependence on magnitude and depth, Geophys. J. Int. 204, 697–718, doi: 10.1093/gji/ggv448.

Parolai, S., and A. Oth (2022). On the Limitations of Spectral Source Parameter Estimation for Minor and Microearthquakes, Bull. Seismol. Soc. Am. 112, 2364–2375, doi: 10.1785/0120220050.

Pezzo, G., P. De Gori, F. P. Lucente, and C. Chiarabba (2018). Pore Pressure Pulse Drove the 2012 Emilia (Italy) Series of Earthquakes. Geophys. Res. Lett. 45, 682–690. doi: 10.1002/2017GL076110.

Picozzi, M., A. Oth, S. Parolai, D. Bindi, G. D. Landro, and O. Amoroso (2017). Accurate estimation of seismic source parameters of induced seismicity by a combined approach of generalized inversion and genetic algorithm: Application to The Geysers geothermal area, California, J. Geophys. Res. 122, no. 5, 3916–3933, doi: 10.1002/2016jb013690.

Prieto, G. A., P. M. Shearer, F. L. Vernon, and D. Kilb (2004). Earthquake source scaling and self-similarity estimation from stacking P and S spectra, J. Geophys. Res. 109, no B08310, 13, doi 10.1029/ 2004JB003084.

Rietbrock, A. (2001). P wave attenuation structure in the fault area of the 1995 Kobe earthquake, J. Geophys. Res. 106, 4141–4154.

Scafidi, D., S. Solarino, and C. Eva (2009). P wave seismic velocity and VP=VS ratio beneath the Italian peninsula from local earthquake tomography, Tectonophysics 465, 1–23.

Scherbaum, F. (1990). Combined inversion for the three-dimensional Q structure and source parameters using microearthquake spectra, J. Geophys. Res. 95, 12,423–12,438.

Scognamiglio, L., L. Margheriti, F. M. Mele, E. Tinti, A. Bono, P. De Gori, V. Lauciani, F. P. Lucente, A. G. Mandiello, C. Marcocci, S. Mazza, S. Pintore, and M. Quintiliani (2012). The 2012 Pianura Padana Emiliana seismic sequence: locations, moment tensors and magnitudes, Ann. Geophys. 55, 549–559.

Shearer, P. M., G. A. Prieto, and E. Hauksson (2006). Comprehensive analysis of earthquake source spectra in southern California, J. Geophys. Res. 111, no. B06303, doi 10.1029/2005JB003979.

Sonley, E., and R. E. Abercrombie (2013). Effects of methods of attenuation correction on source parameter determination, in Earthquakes: Radiated Energy and the Physics of Faulting, R. Abercrombie, A. McGarr, G. Di Toro, and H. Kanamori (Editors), 91–97, doi: 10.1029/170GM11.

Stachnik, J. C., G. A. Abers, and D. H. Christensen (2004). Seismic attenuation and mantle wedge temperatures in the Alaska subduction zone, J. Geophys. Res. 109, doi: 10.1029/2004JB003018.

Stein, S., and M. Wysession (2009). An introduction to seismology, earthquakes, and earth structure, in Earthquakes, Wiley-Blackwell Publishing, Oxford, United Kingdom, ISBN: 978-1-4443- 1131-0.

Strollo, A., D. Cambaz, J. Clinton, P. Danecek, C. P. Evangelidis, A. Marmureanu, L. Ottemöller, H. Pedersen, R. Sleeman, K. Stammler, et al. (2021). EIDA: The European integrated data archive and service infrastructure within ORFEUS. Seismol. Res. Lett. 92, no. 3, 1788–1795, doi: 10.1785/0220200413.

Toomey, D. R., and G. R. Foulger (1989). Tomographic inversion of local earthquake data from the Hengill-Grensdalur central volcano complex, Iceland. Journal of Geophysical Research 94, 17,497–17,510.

Trugman, D. T., and P. M. Shearer (2017). Application of an improved spectral decomposition method to examine earthquake source scaling in southern California, J. Geophys. Res. 122, no. 4, 2890–2910, doi: 10.1002/2017JB013971.

Tsumura, N., A. Hasegawa, and S. Horiuchi (1996). Simultaneous estimation of attenuation structure, source parameter, and site response spectra—application to the northeastern part of Honshu, Japan, Phys. Earth Planet. Inter. 93, 105–121.

Tsumura, N., S. Matsumoto, S. Horiuchi, and A. Hasegawa (2000). Three-dimensional attenuation structure beneath the northeastern Japan arc estimated from spectra of small earthquakes, Tectonophysics 319, 241–260.

Valoroso L. Chiaraluce L. Piccinini D. Di Stefano R. Schaff D. Waldhauser F. (2012). Radiography of a normal fault system by 64,000 high-precision earthquake locations: The 2009 L'Aquila (central Italy) case study, J. Geophys. Res. 118, 1–21.

Yoshimitsu, N., W. L. Ellsworth, and G. C. Beroza (2019). Robust stress drop estimates of potentially induced earthquakes in Oklahoma: Evaluation of empirical Green's function, Journal of Geophysical Research: Solid Earth, 124, 5854–5866. https://doi.org/10.1029/2019JB017483.

Wang, H., Y. Ren, R. Wen, and P. Xu (2019). Breakdown of earthquake self-similar scaling and source rupture directivity in the 2016–2017 central Italy seismic sequence, J. Geophys. Res. 124, 3898–3917, doi: 10.1029/2018JB016543.

Wessel, P., W. H. Smith, R. Scharroo, J. Luis, and F. Wobbe (2013). Generic mapping tools: Improved version released, Eos Trans. AGU 94, no. 45, 409–410.

Wiemer, S., and M. Wyss (2000). Minimum magnitude of complete report- ing in earthquake catalogs: Examples from Alaska, the western United States, and Japan, Bull. Seismol. Soc. Am. 90, 859–869, doi: 10.1785/ 0119990114.

Zollo, A., A. Orefice, and V. Convertito (2014). Source parameter scaling and radiation efficiency of microearthquakes along the Irpinia fault zone in southern Apennines, Italy, J. Geophys. Res. 119, 3256–3275, doi: 10.1002/2013JB010116.

Author's affiliation and corresponding author's email address

Pasquale De Gori (corresponding author): pasquale.degori@ingv.it
INGV, via di Vigna Murata 605, 00143, Rome.

Francesco Pio Lucente: pio.lucente@ingv.it
INGV, via di Vigna Murata 605, 00143, Rome.

Claudio Chiarabba: claudio.chiarabba@ingv.it
INGV, via di Vigna Murata 605, 00143, Rome.

List of Figure Captions

Figure 1. (a) Spatial distribution of the aftershocks used in this work. Hypocentral depths are differentiated by the color code while the circle size is proportional to the event magnitude according to the scheme on the left of the map. The largest (M>=5.0) events are drawn by stars. The two mainshocks are also indicated by the TDMT focal plane solutions (Scognamiglio et al., 2012). Black and gray triangles are respectively the permanent and temporary seismic stations operating in the area during the 2012 Emilia seismic sequence. (b) Frequency–magnitude distribution (FMD) of the used aftershocks. The cumulative and non-cumulative numbers of earthquakes are shown by light gray squares and dark gray triangles, respectively. The gray dashed line indicates the completeness magnitude value (2.1), while the black line represents the maximum likelihood fit to the data for magnitudes above the magnitude of completeness at 95% level (Wiemer and Wyss, 2000), whose slope is the b-value of the Gutenberg-Richter law.

Figure 2. (a) Site responses for P and S spectra fit for the representative stations 0812, 0824, and RAVA. The first two stations are temporary while the last one is permanent. Gray lines indicate individual response functions, counted by the number reported close to the station's name. The black lines indicate the mean site response function while dotted lines indicate the associated error quantified by one standard deviation. (b) P and S stations residuals, resulting from the 3D velocity inversion of Pezzo et al. (2008), against the mean value of site response in the frequency interval 10-20 Hz. On the upper panel we observe that station residuals from P model and site response are characterized by a chaotic disposition of data points, conversely, on the lower panel, for S waves we observe that station residuals and site response exhibit a weak positive correlation, as evidenced by the straight-line fit of the data (black dashed line in the lover panel), having a slope of 0.38 and a coefficient of linear regression of 0.40.

Figure 3. (a) Trade-off curves used to select the damping parameters for the inversions of Qp (top) and Qs (bottom) tomographic models. On both curves, the bigger black dot indicates the chosen damping value. (b) Qp and Qs models at horizontal slices located at 3, 6 and 9 km depth. This depth interval hosts the main seismogenic volume of the sequence. The strong heterogeneities of Qp and Qs crustal structure results in very different attenuation terms used to correct the observed spectra before the computation of source parameters. The black dashed lines show the well-resolved region of the model with Spread Function < 3 as defined by Michelini and McEvilly (1991) (see also Toomey and Foulger, 1989). White stars indicate the first and the second main shocks in the layers at 6 and 9 km depth, respectively (M_L=5.9, 2012-05-20, hh 02:03 UTC; M_L=5.8, 2012-05-29, hh 07:00 UTC); the gray dots are the aftershocks.

Figure 4. Source parameters determined from the fit of P (left) and S (right) spectra. For each phase, the Seismic Moment vs source radius (top), Seismic Moment vs Stress Drop (middle) and Moment Magnitude vs Corner Frequency (bottom), are reported. Aftershocks are drawn by circles sized and colored on the basis of their magnitude according to the legend on the bottom panels. Stars are M5+ events. On the upper and bottom panels, black lines refer to constant stress drop values expressed in MPa.

Figure 5. (a) Histograms showing the frequency distribution of P-stress drop (left), S-stress drop (middle) and of the ratio between P and S waves stress drop (right). On the top of each histogram the mean and the standard deviation of the log normal distribution is reported. (b) Histogram of the ratio between the P-and the S-source corner frequency. In log space, the average ratio is 0.23+/- 0.09 that leads to a mean (f_cP/f_cS) of 1.70 with a confidence interval between 1.37 and 2.10.

Figure 6. Local (M_L) against the Moment Magnitude (Mw) deriving from P- (left) and S-waves (right) spectra fit. The gray lines indicate M_L=Mw. The dashed lines are the results of the orthogonal regression of our M_L-Mw data performed minimizing the distance between each data point and the resulting line. This approach should be preferred to the standard regression strategies when data are affected by unknown uncertainties (in our pool of data this is the case of M_L; Golub and van Loan, 1980). In the title of each plot we report the details of the fitting line: the slope (m), its error as well as the intercept (q) and its uncertainty.

Figure 7. Misfit function (MF) deriving from the P-f_c grid-search of one event of M_L=2.2; In both (a) and (b) panels, the gray inset shows a zoom around the minimum (left); histogram of the bootstrap resampling shows the distribution of the recovered f_c (right). Titles on the left plots report the final value of f_c with its absolute and relative error while, on the right, the f_c, along with the associated standard deviation deduced by the bootstrap histogram, is indicated. In (a) spectra are processed with any a-priori assumptions (Step-01 of the workflow) while in (b) spectral fit are carried out fixing the spectral attenuation to the values extracted by the 3D Q model. It is noteworthy that: in (a) we could not identify a clear minimum of the MF although the inset show that it numerically exists; the bootstrap histogram is also irregular showing a blurred f_c distribution; in (b) we observe a well picked minimum in the misfit curve and well-shaped frequency distribution of the bootstrap f_c.

Figure 8. MF deriving from the S-f_c grid-search of the same event of M_L=2.2 of Figure 7; see other details in the caption of Figure 7.

Figure 9. Cumulative histograms showing the distribution of stress drop relative errors as obtained for P- (upper panels) and S-waves (lower panels) spectral fit. Left and central panels refer to errors computed in the part-01 and part-02 of the workflow, respectively. On the right panels, errors are related to spectral fit where tomo Q is used to correct attenuation. As title, the total number of events is reported. In each panel, the dashed vertical line indicates the 30% of the stress drop error values. Note that, by using Q tomography, we get final stress drop errors within 30% for the 80% of the events and the number of usable events for source parameter consideration is sensibly higher.

Figure 10. Comparison of Stress Drop computed by spectral fit and coda wave approach. Larger circles represent the master events of each cluster (all in the magnitude interval 3-4). Each small gray point represents EGF belonging to at least 2 clusters. (a) Comparison between absolute values of stress drop. The gray line indicates equal values of stress drop. The dashed line represents the linear fit of data: slope = 0.87, intercept = 1.05. (b) Comparison of stress drop variation with respect to the mean value by using the same datasets of (a). Gray dashed lines indicate null variations with respect to the average stress drop.

Table

TABLE 1

Number of events selected in the 3 steps of the workflow

Step → / **Magnitude Ranges ↓**	**Step-01**	**Step-02**	**Step-03**
2-3 P-waves	234 (205)	415 (393)	1074 (1061)
3-4 P-waves	95 (95)	138 (138)	143 (143)
4-5 P-waves	5 (5)	6 (6)	3 (3)
2-3 S-waves	665 (663)	785 (785)	1029 (1029)
3-4 S-waves	136 (136)	146 (146)	134 (134)
4-5 S-waves	8 (8)	9 (9)	9 (8)

Table 2

TABLE 2

Frequency Bands and Magnitude Ranges in the 3 steps of the workflow

Step → / **Magnitude Ranges ↓**	**Part-01 (site-corr)**	**Part-02 (t* for tomoQ)**	**Part-03 (source par)**
2-3 (1.28 s)	1-40 Hz (all band)	1-40 Hz (30)	1-40 Hz (30)
3-4 (2.56 s)	0.2-40 Hz (all band)	0.2-40 Hz (30)	0.2-40 Hz (30)
4-5 (5.12 s)	0.1-40 Hz (all band)	0.1-40 Hz (30)	0.1-40 Hz (30)
5-5.5 (10.24 s)	0.05-40 Hz (20): single step		
5.8-6.0 (Mainshocks, 40.96 s)	0.03-30 Hz (20): single step		

Figure 1

Click here to ac

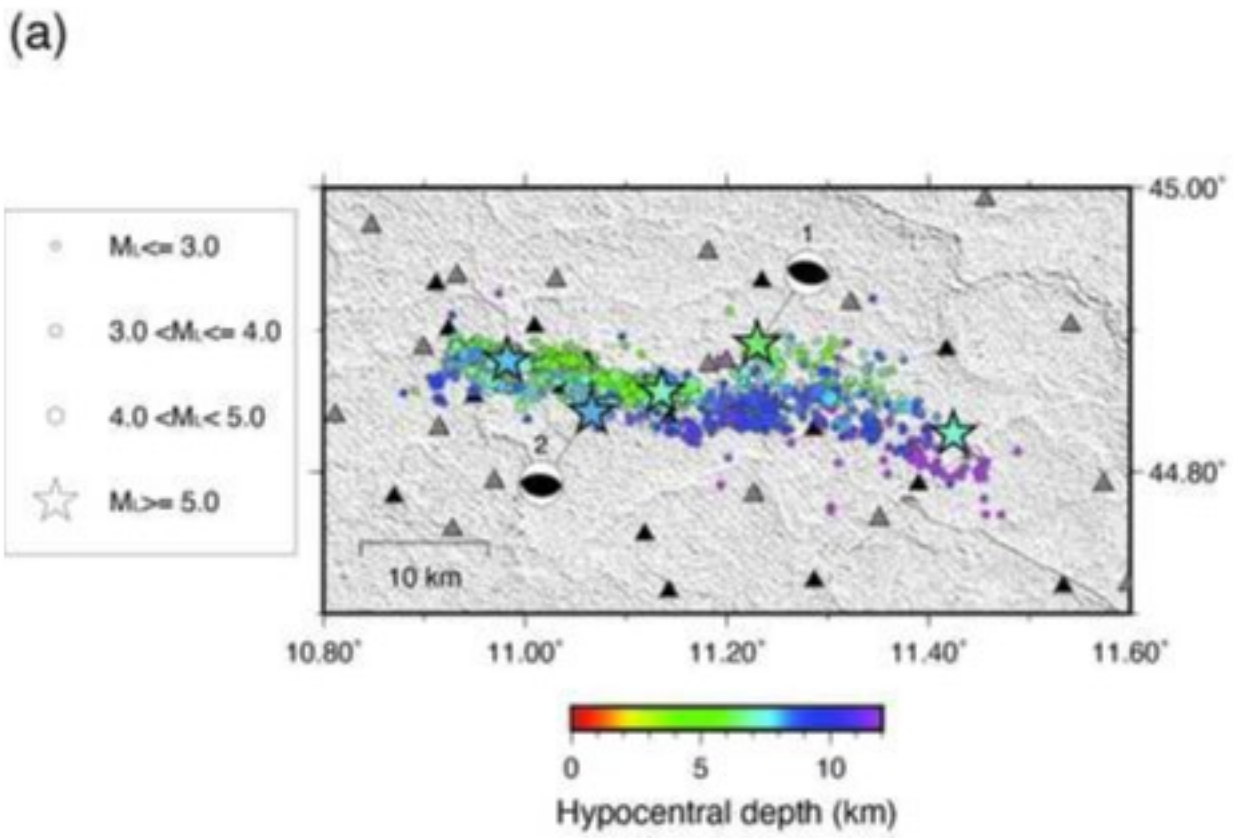

Figure 2

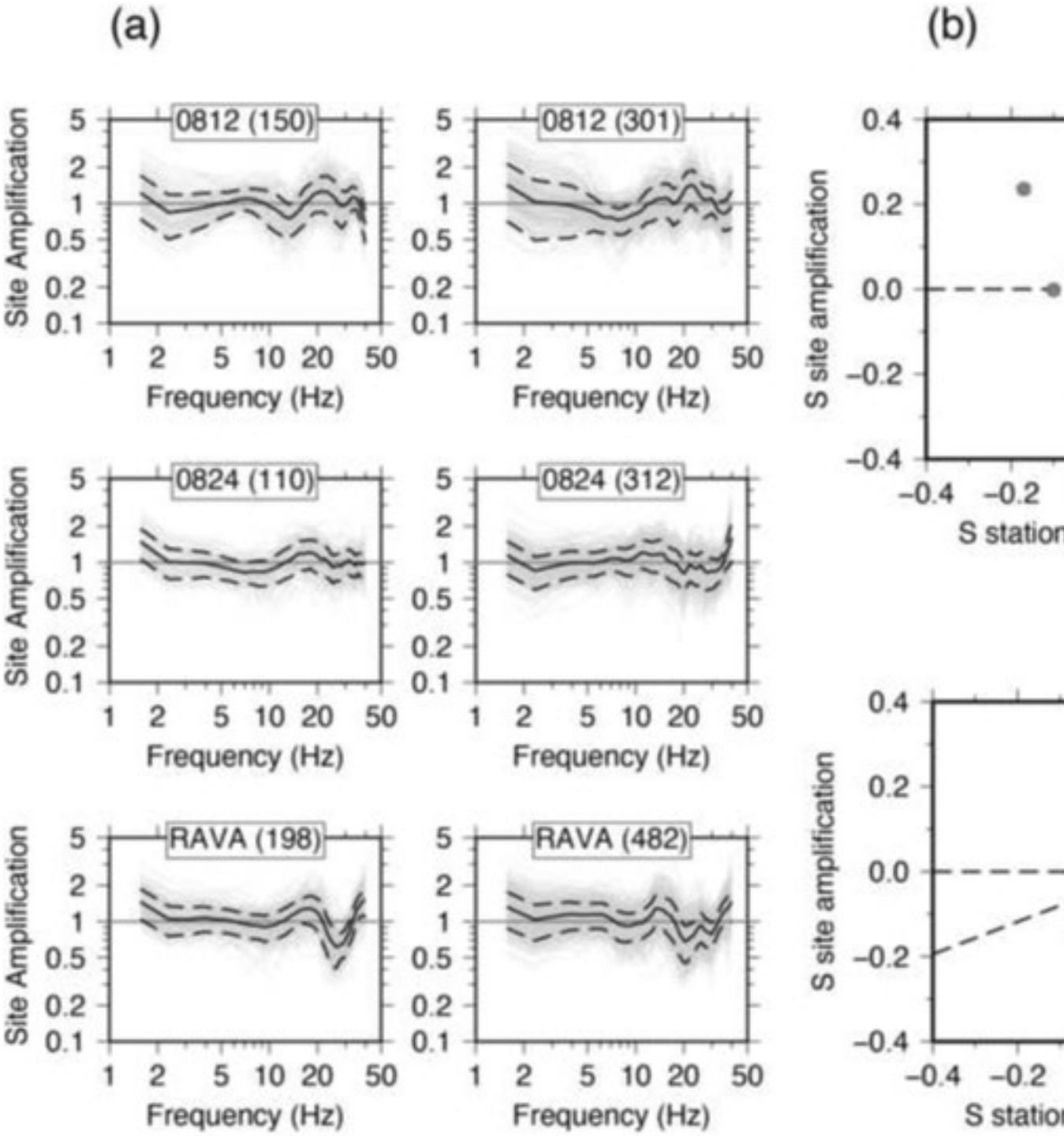

Figure 3

Click here to access

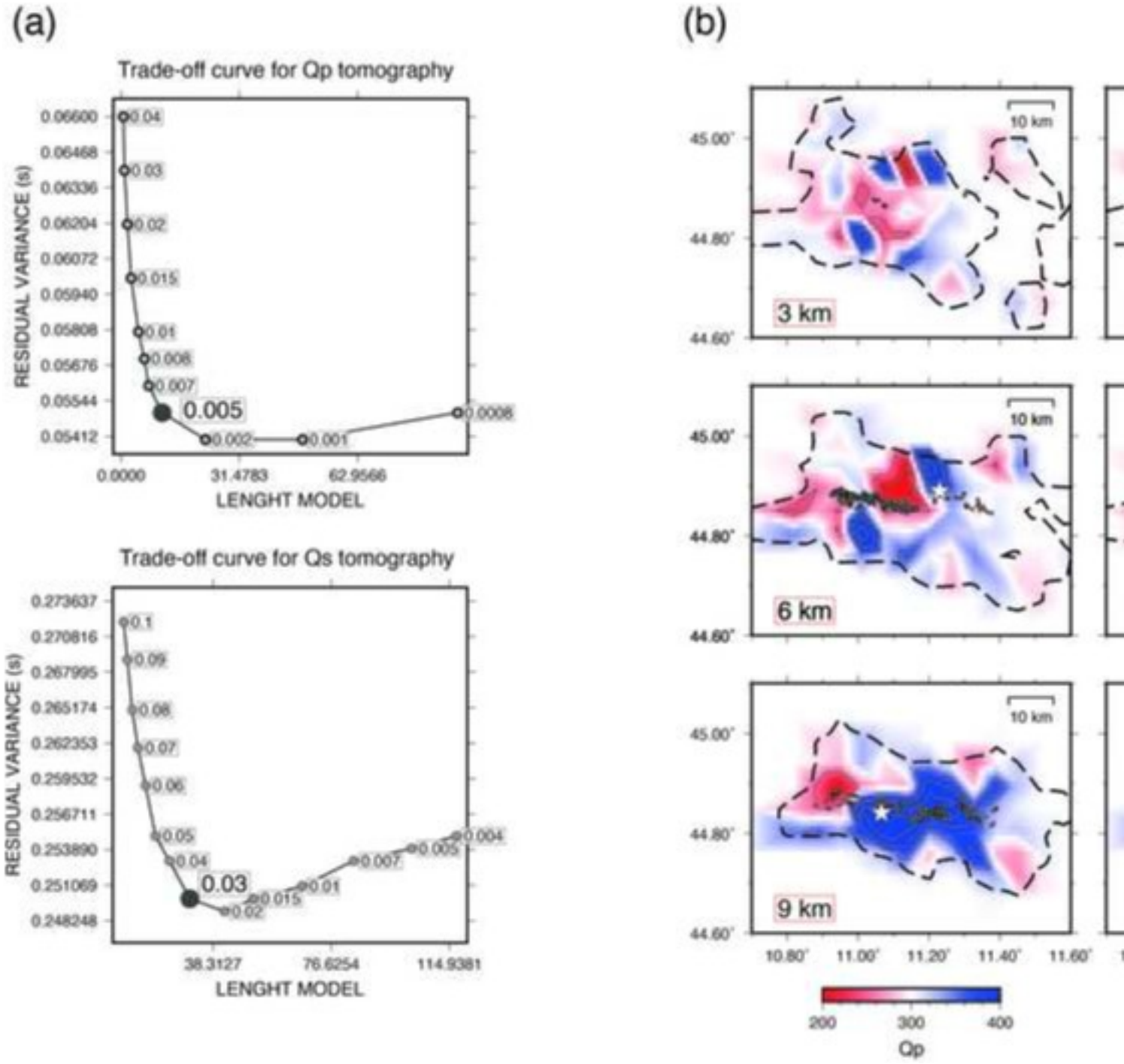

Figure 4

Click here to access/download;Figure;Fig-04-P+S_Source_time-scaled.jpg

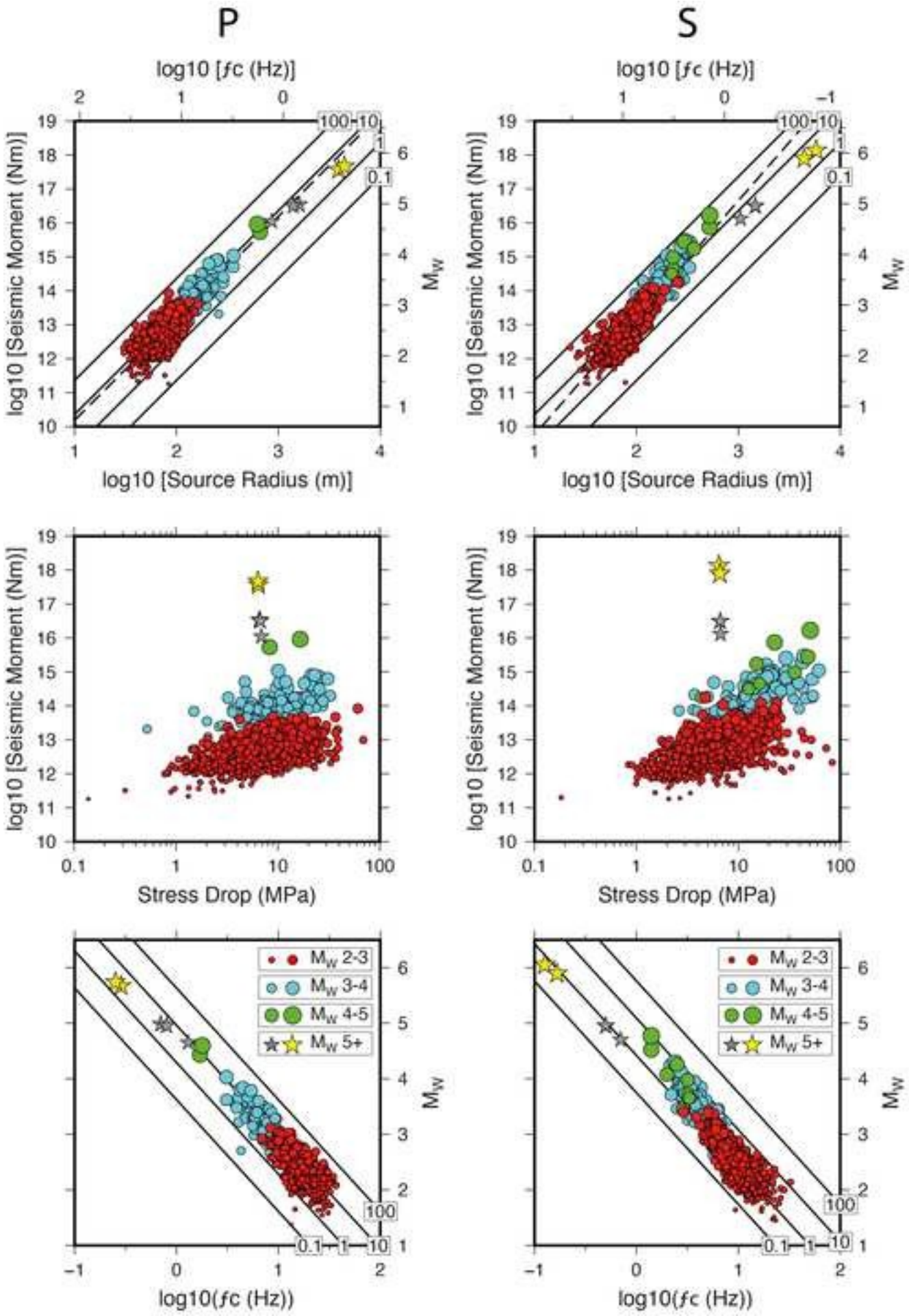

Figure 5

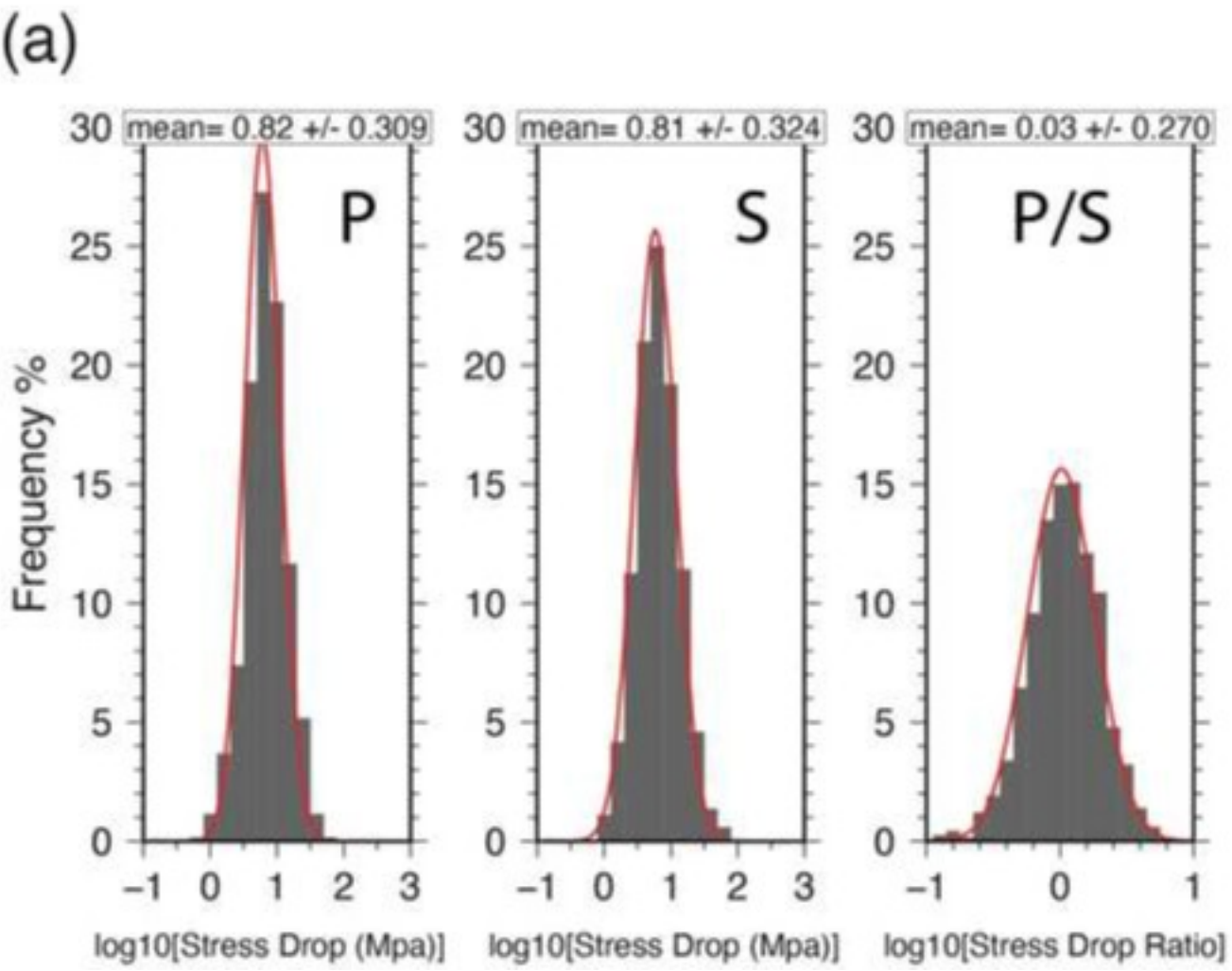

Figure 6

Click here to acces

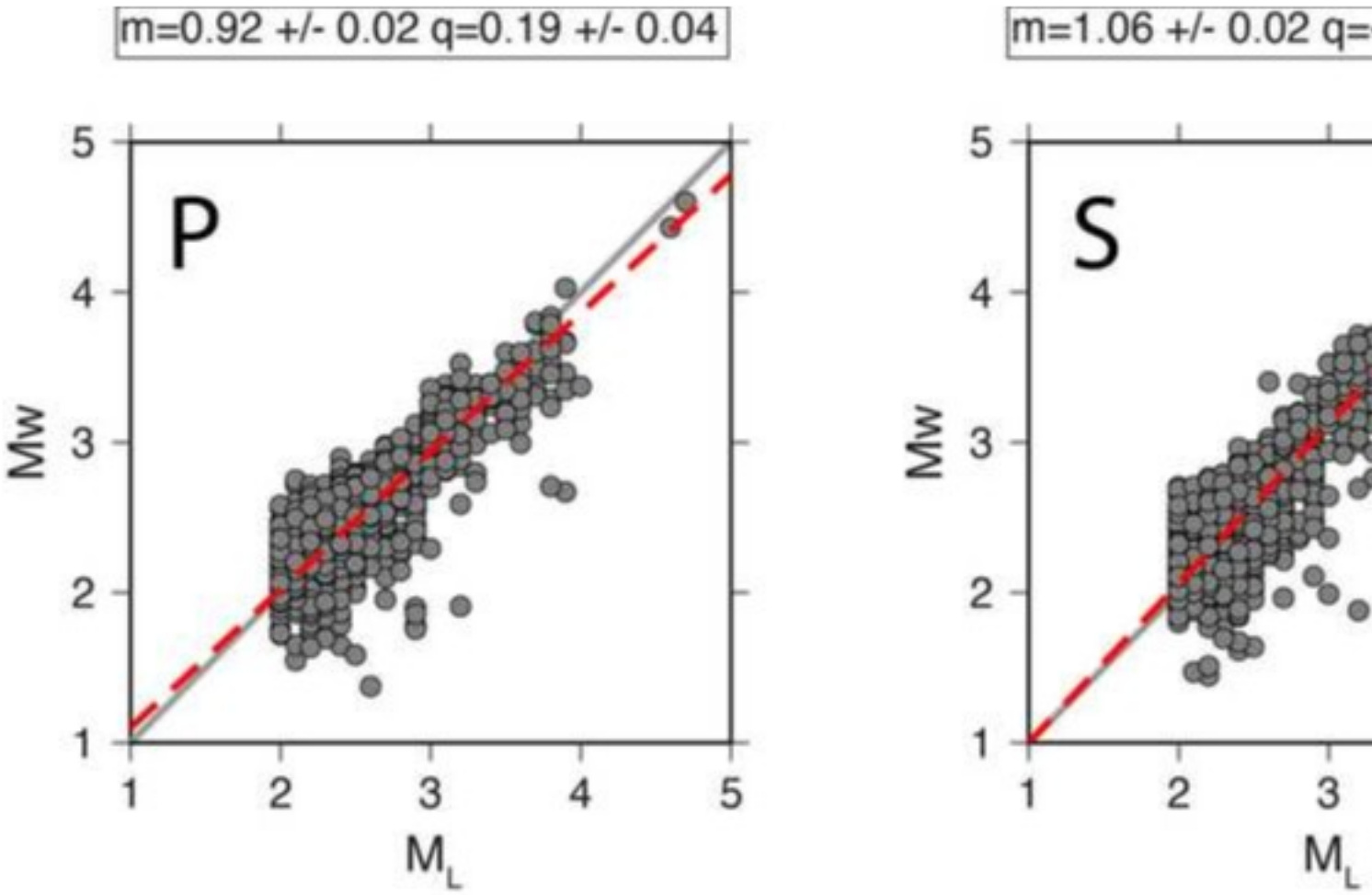

Figure 7

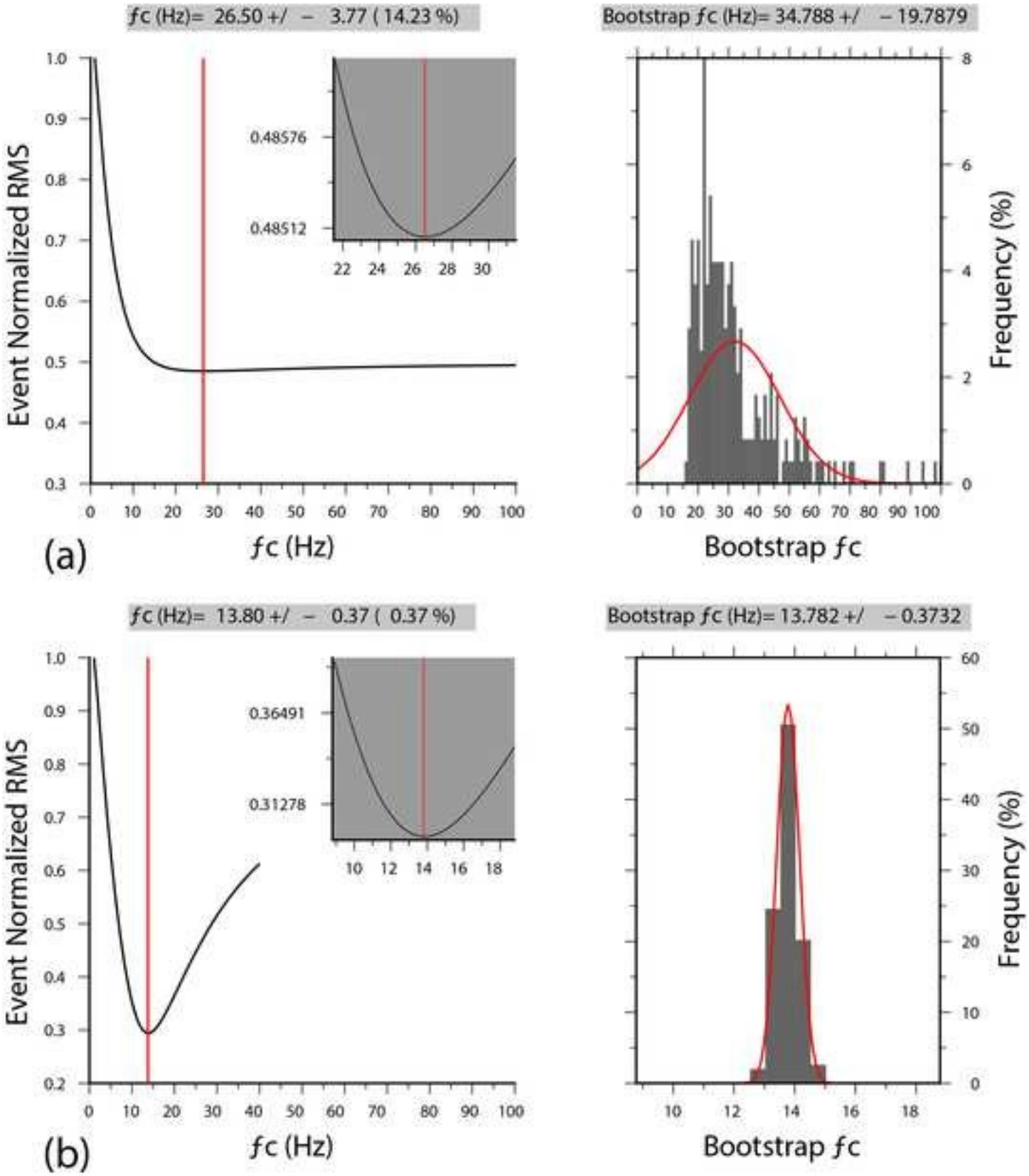

Figure 8

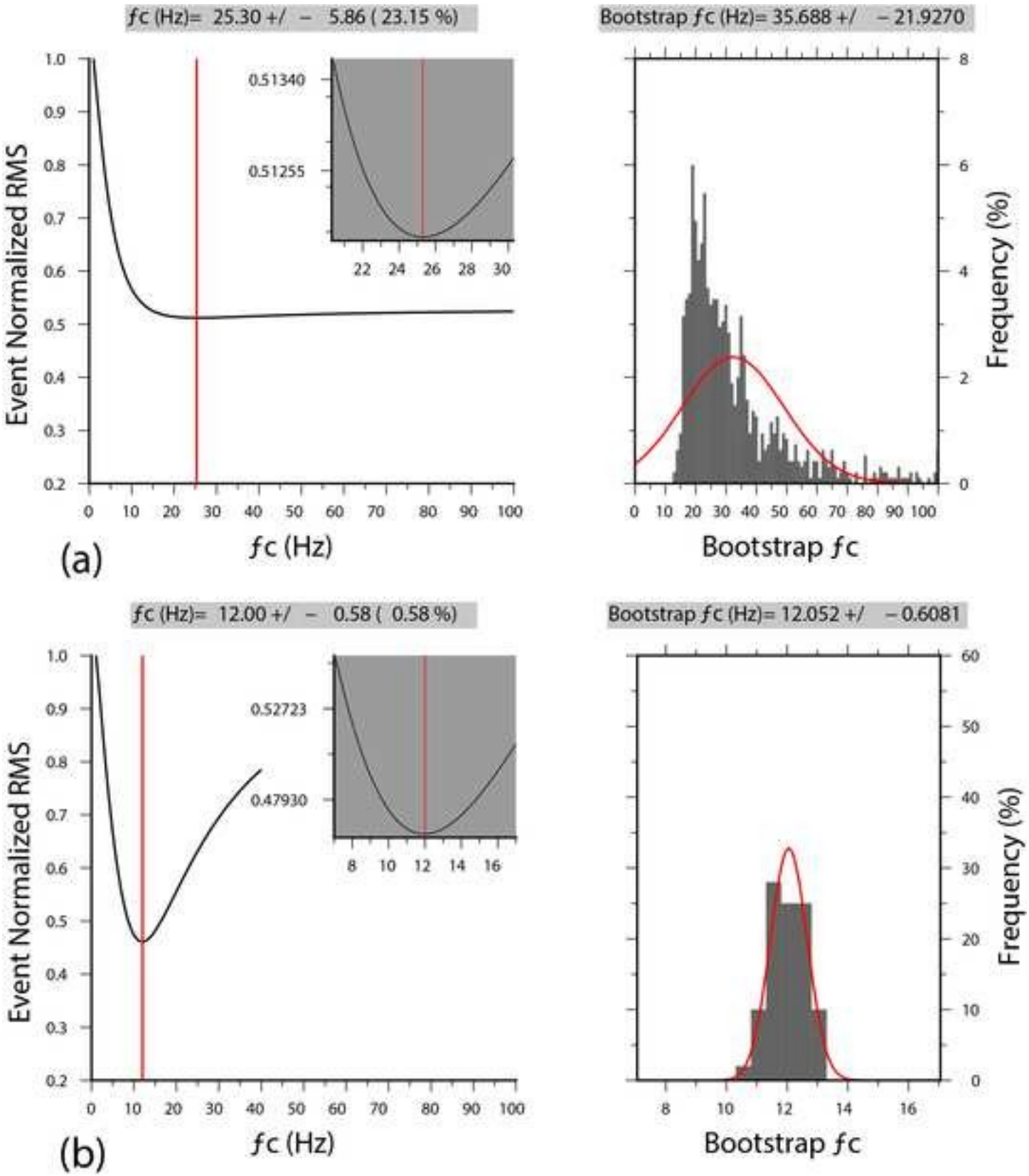

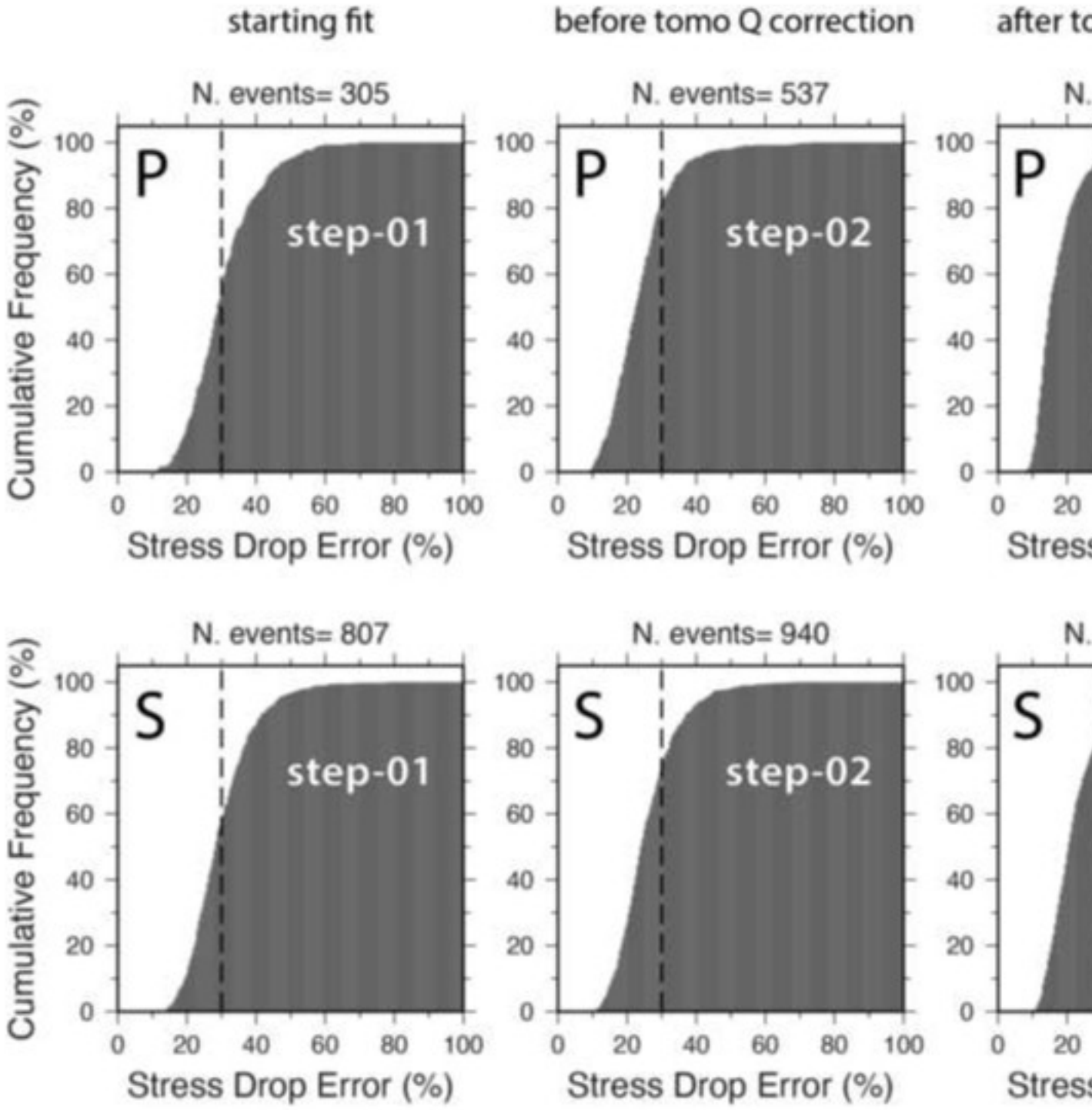

Figure 10

Click here to access/download;Figure;Fig
sdrop.jpg

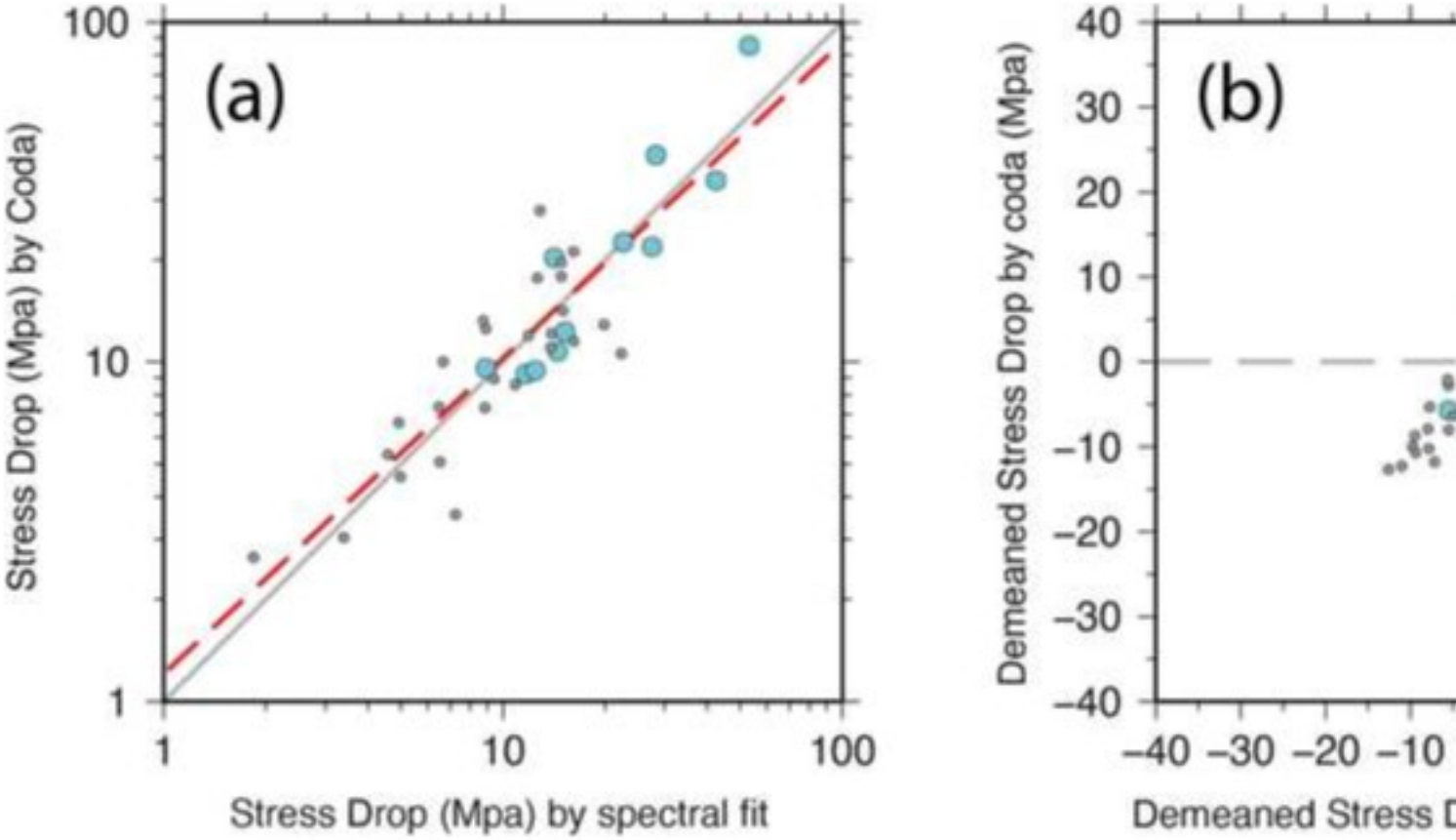

Supplemental Material for

Source parameter estimation after attenuation correction through the use of Q

This supplement contains additional material on the dependency of the quality factor (Q) from the frequency, on the error analysis on source parameter estimation, and on the comparison of Stress-Drop estimations by direct S– and coda–waves fit. Furthermore, it contains examples of spectral fit for lower magnitude events and of the fitting procedure in the three different steps of the workflow described in the main text for the P- and S-waves, respectively.

1. On the frequency dependence of t* and quality factor (Q)

The dependency of quality factor from the frequency is quantified in equation 3 of the main text by the α exponent that it could assume values from 0 to 1. $\alpha > 0$ leads to higher attenuation (high t*, low Q values) for low frequencies leaving the highest frequencies less attenuated. The use of frequency-dependent Q (i.e. varying the α values) would imply several attenuation models, one for each selected frequency (e.g. Koulakov et al. 2011).

In order to check the dependency of the attenuation from the frequency, we run several fit varying α between 0 and 1 at 0.1 step, for the whole P and S dataset at the first step of the workflow. In Figure S1 we report, for each class of magnitude, the global RMS obtained by using P and S spectral fits. We observe that in the class of magnitude 2-3, the most populated subset of events (Table 1 of the main text), both P- and S-waves spectral fits are characterized by a direct relationship among RMS and α. Therefore, we obtain the best fits for t* (and quality factor) that are frequency independent. In the class of magnitude 3-4, we observe a substantial flattening of the curves for P- and S- waves fit for α ranging from 0.1 to 0.4. For α > 0.4 we then observe a gradual increasing trend. In the class of magnitude 4-5, the observed behavior is sensibly different. In fact, we get a minimum of RMS with α equal to 0.4 and 0.5 for P- and S-wave spectra fits, respectively, suggesting a frequency dependence of attenuation. Since the majority of analyzed events belongs to the magnitude classes 2-3 and 3-4 (see Table 1), we are confident that setting $\alpha = 0$ is a licit assumption as already stated in previous studies based on attenuation tomography (Boatwright et al., 1991; Rietbrock, 2001; Edwards et al., 2008). We are also aware that when the used dataset is dominated by aftershocks with magnitude

above 4, the Q frequency dependent should be accounted for. Our observed trends (Figure S1) are in general agreement with previous studies and indicate a weak frequency-dependence of attenuation for low magnitude events and a clear dependency for magnitude above 4.

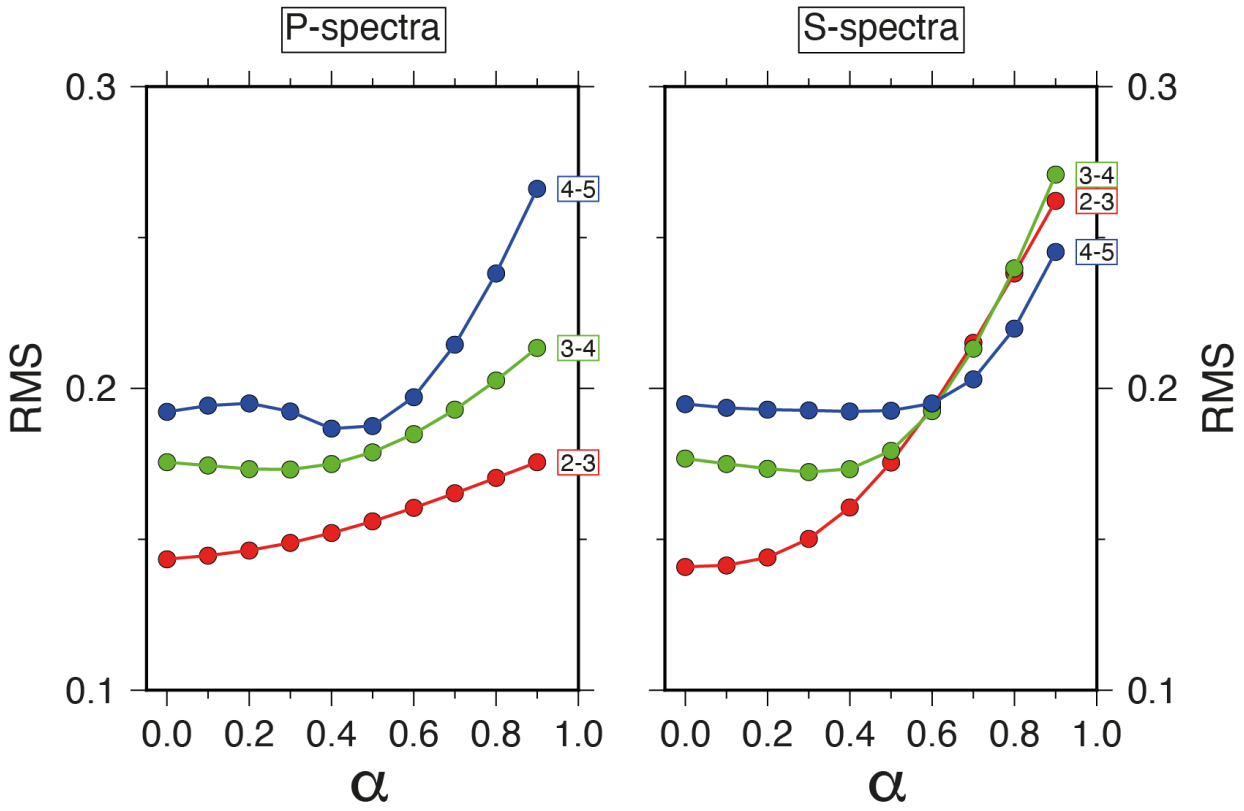

Figure S1. Overall RMS fit for P (left) and S-waves (right) spectra by using different value of α (see equation 3 in the main text) for different magnitude classes of earthquakes (red: M_L=2-3, green: M_L=3-4, blue: M_L= 4-5).

3. Examples of the fitting procedure in the three different steps of described in the main text for the P- and S-waves, respectively

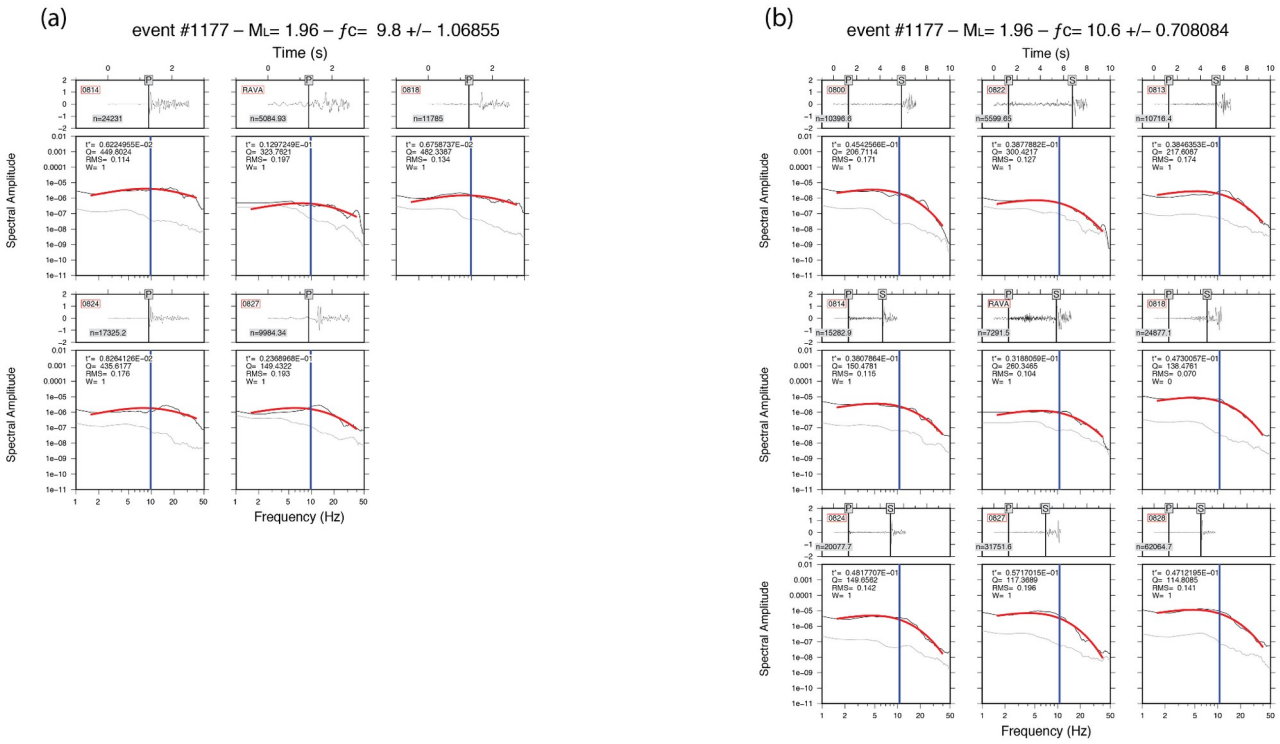

Figure S2. (a) Example of fit of P-waves spectra relative to a $M_L \approx 2.0$ event processed in the step-01 of the workflow. For each station we show the seismogram (top) with the relative spectra (below). On the time series the vertical black line marks the phase onset from which we extract the signal and the noise time window (see Dataset section in the main text). The label on the upper-left indicates the station name while on the bottom left we report the seismogram normalization factor that is used only for plot purposes. On the spectra plot we show the signal and the noise spectrum by the black and gray line, respectively. The red line represents the fit to the portion of the signal spectrum characterized by an adequate S/N. The vertical bar indicates the corner frequency, common to all the stations of the event. Furthermore, t* (and Q) indicates the high frequency spectral decay while W, calculated using the RMS between observed and computed spectral amplitudes, quantifies the goodness of the fit (0= best fit, 4=worst fit). (b) the same as (a) but for the fit of S-waves spectra of the same event.

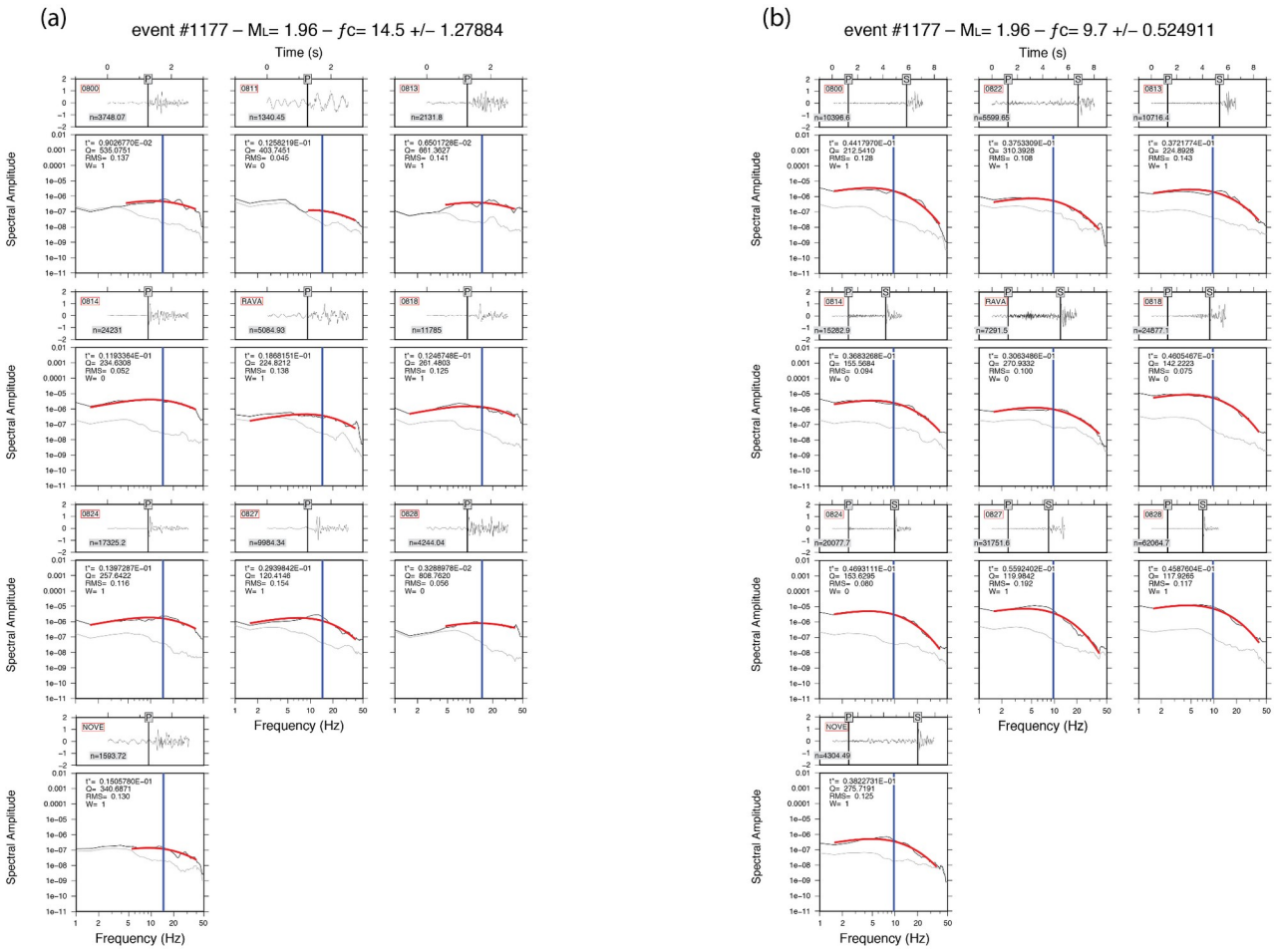

Figure S3. Example of fit of P- (a) and S-waves (b) for one event processed in the step-02 of the workflow. For explanation about the panel showing the seismogram and the spectra, see details in the caption of Figure S2.

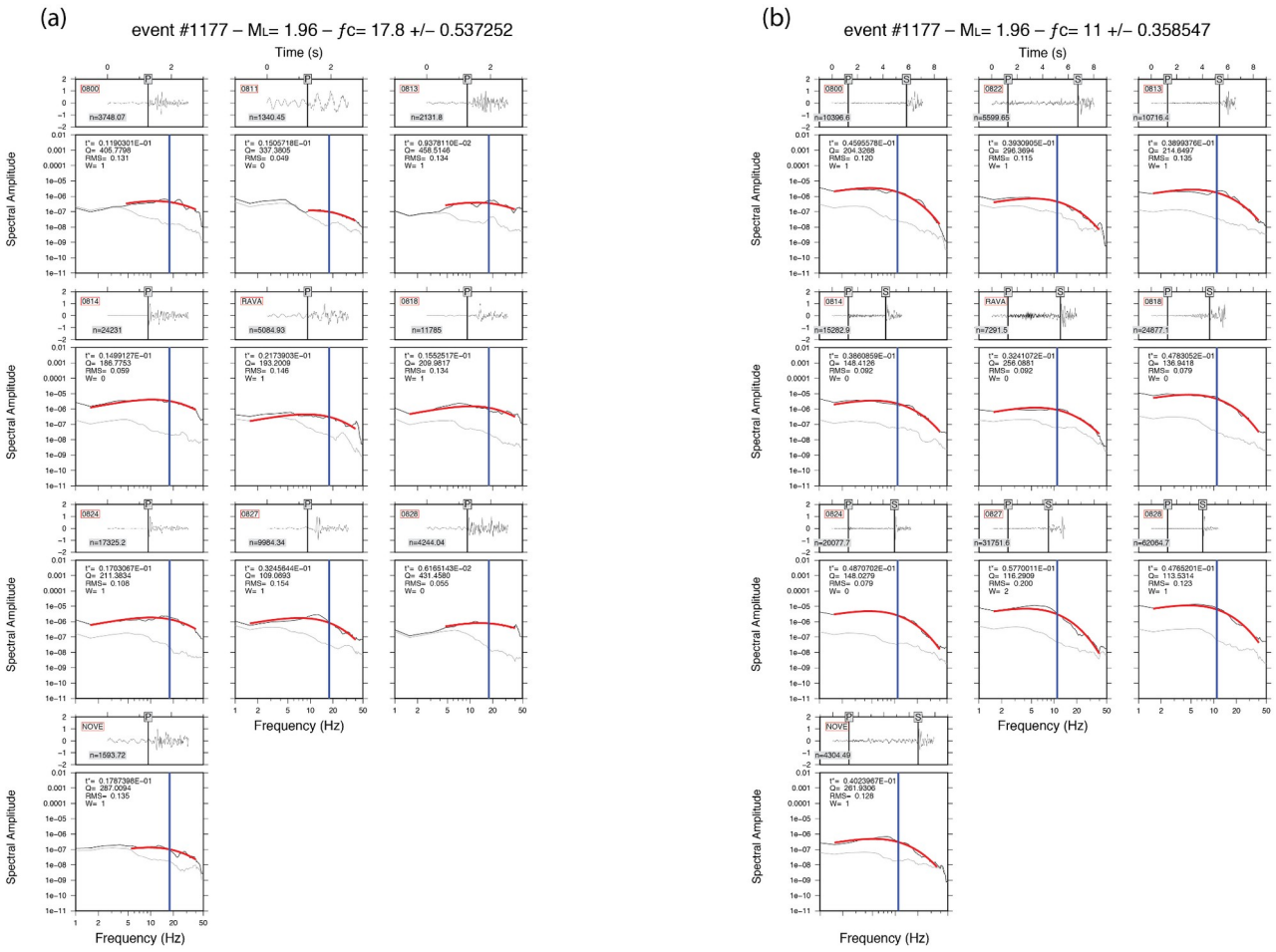

Figure S4 Example of fit of P- (a) and S-waves (b) for one event processed in the step-03 of the workflow. For explanation about the panel showing the seismogram and the spectra, see details in the caption of Figure S2.

4. Error analysis on source parameter estimation for events of magnitude M_L=3-4 and M_L=4-5

As stated in the main text, and demonstrated in the below Figures S5-S8, at increasing magnitude, the effect of the attenuation correction is progressively less significant, due to the greater content of low-frequency energy in the seismic signals.

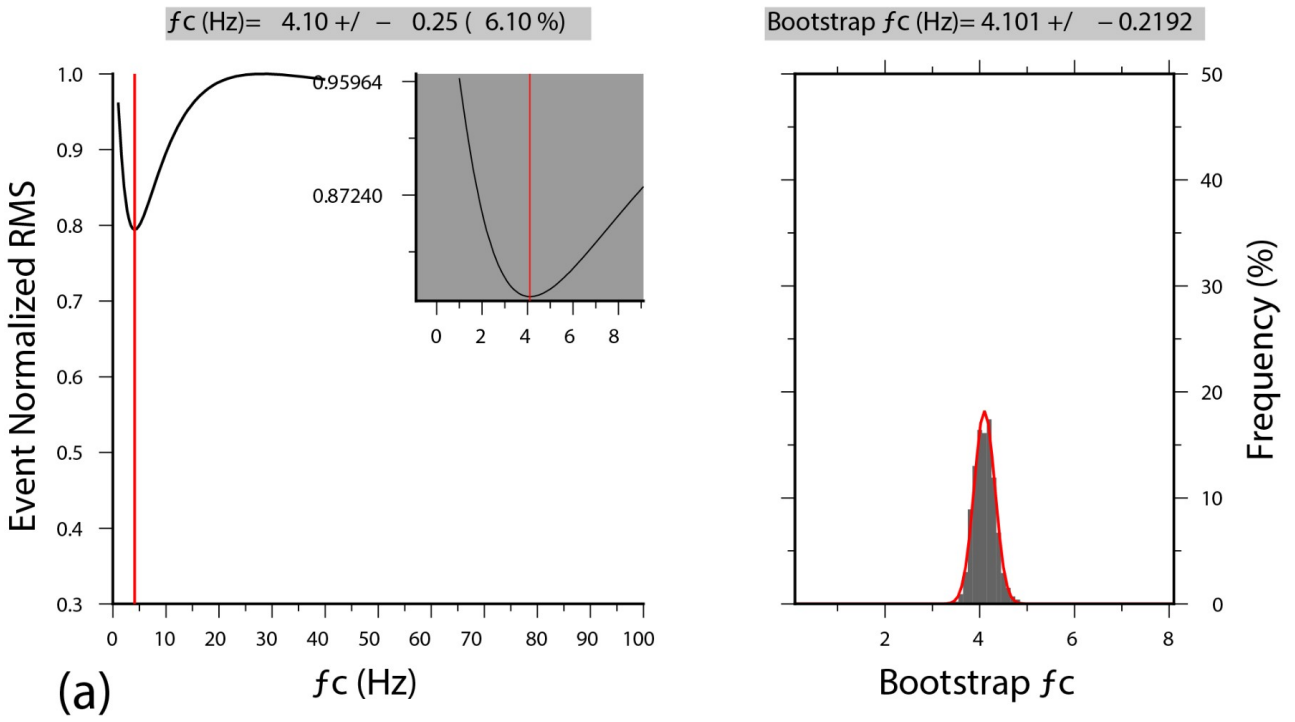

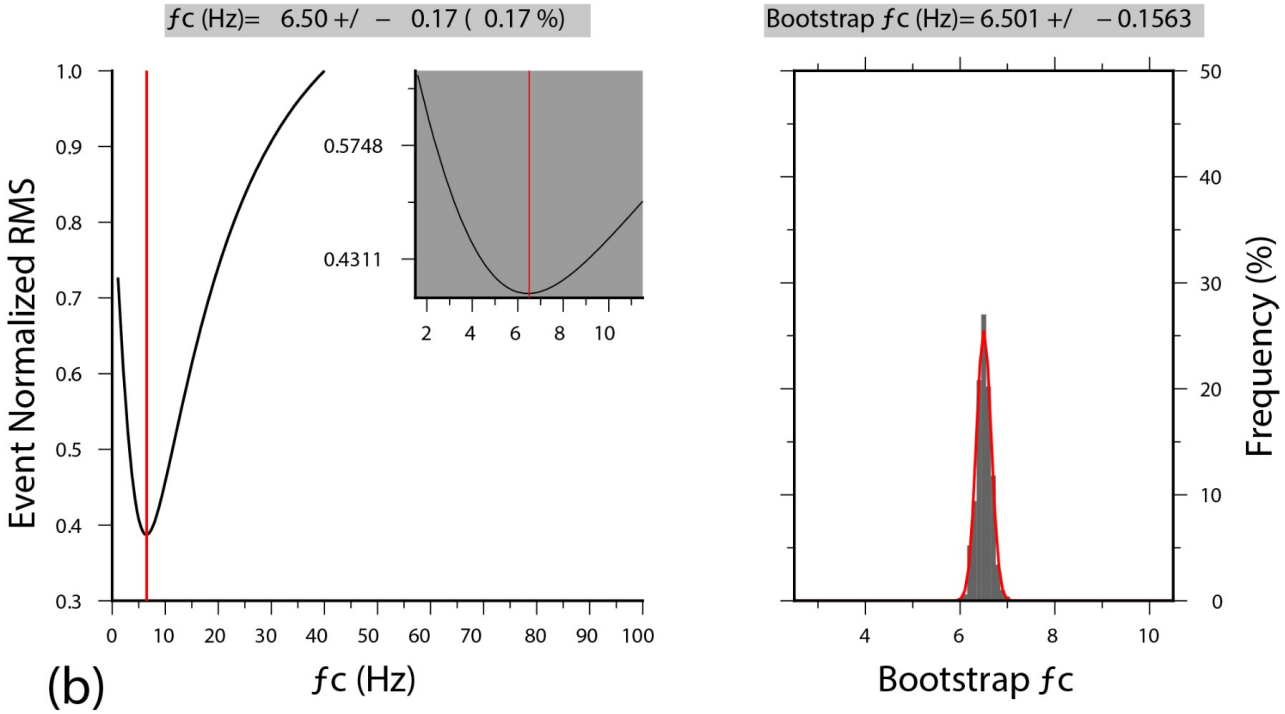

Figure S5 MF from the P-fc grid-search of one event of M_L=3.9; the meanings of the panels and symbols are the same as in Figure 7 of the main text. It is noteworthy that both a) and b) MF curves are characterized by a clear minimum. In b) the MF curve bottoms at a lower value of RMS indicating that tomo Q corrections lead to an improved fit.

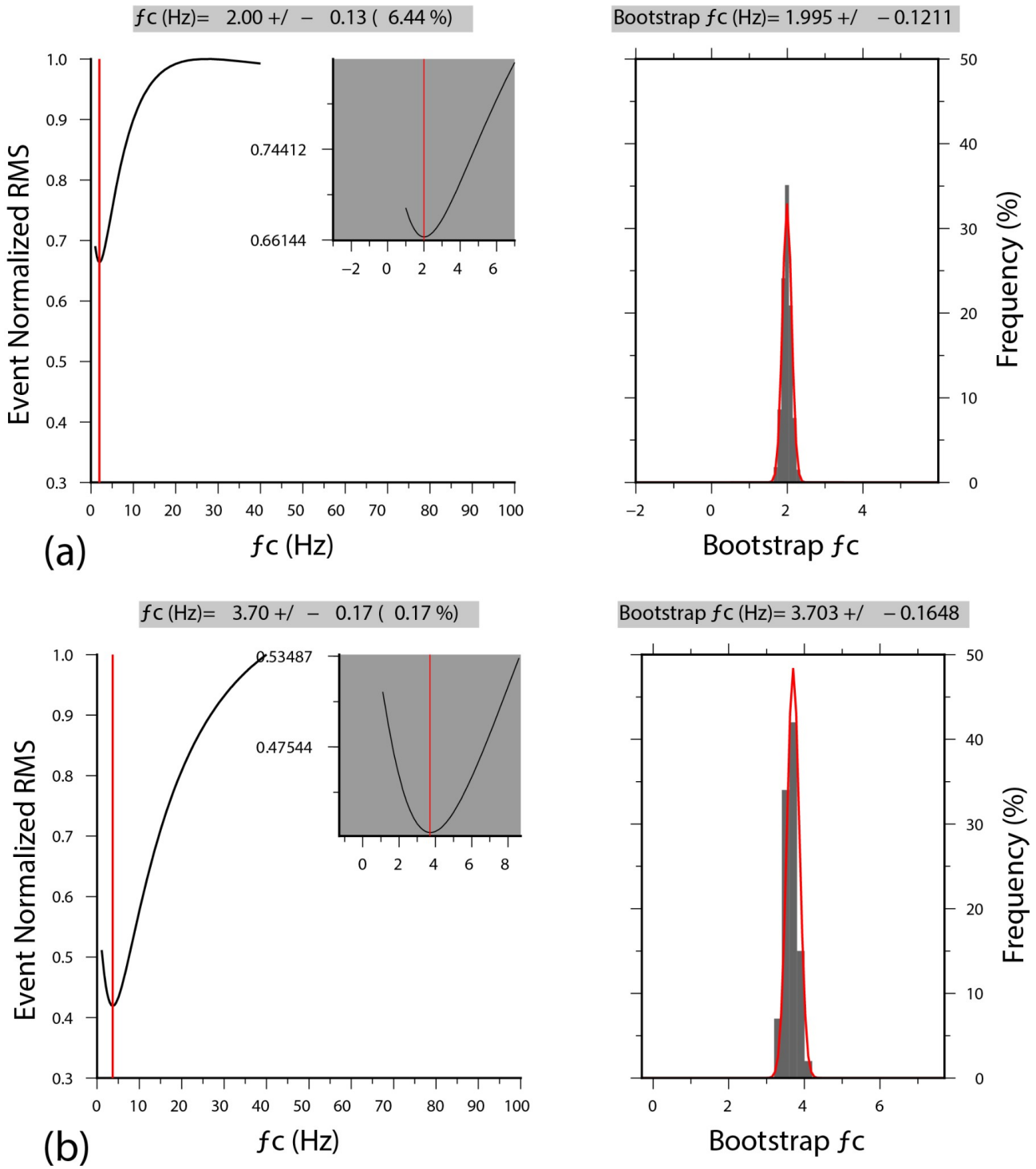

Figure S6. MF from the S-fc grid-search of the same event of M_L=3.9 of Figure S5; the meanings of the panels and symbols are the same as in Figure 8 of the main text. As for P-waves spectra fit (Figure S5), both (a) and (b) MF curves are characterized by a clear minimum. In (b) the MF curve bottoms at a lower value of RMS indicating that tomo Q corrections lead to an improved fit.

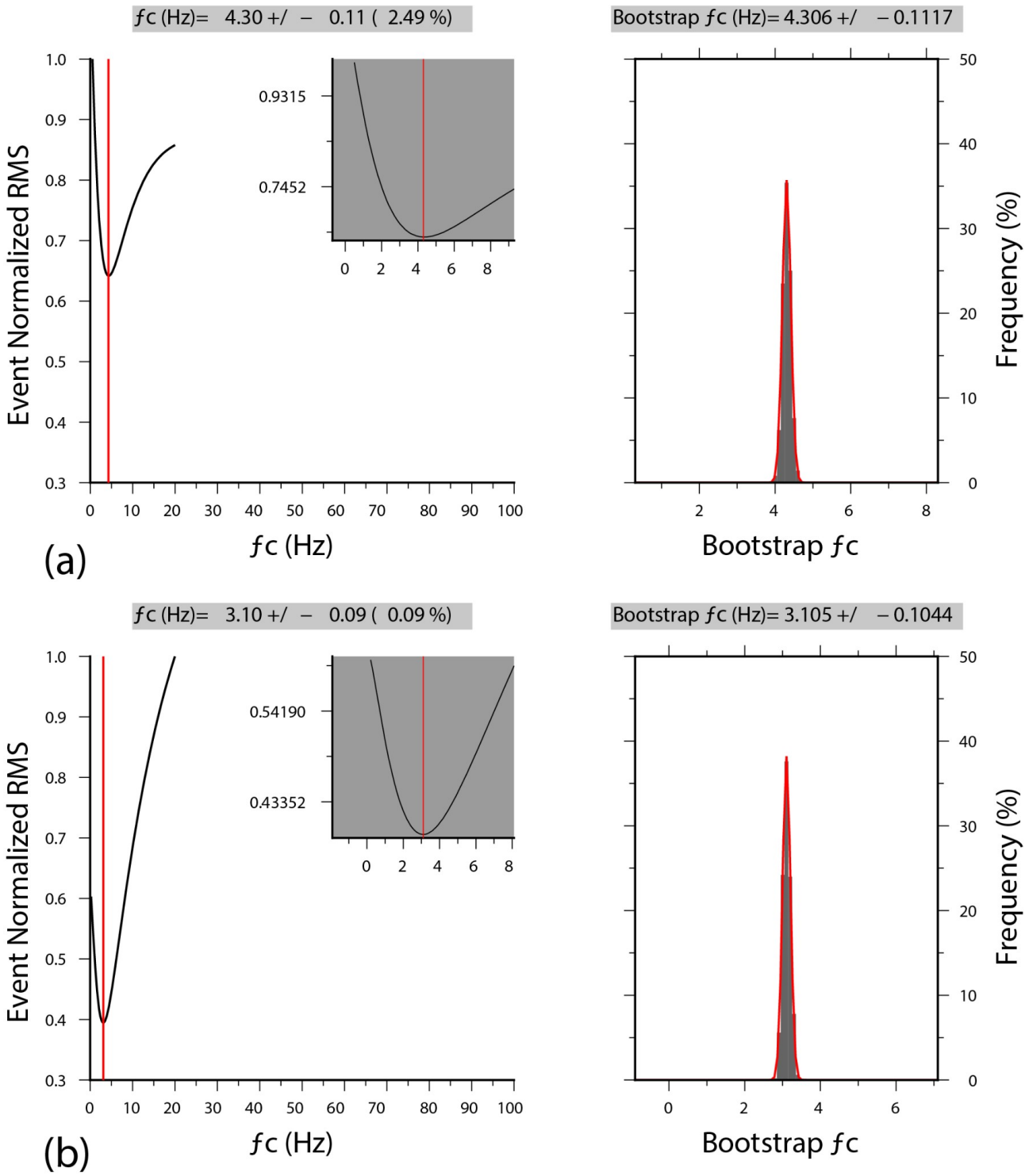

Figure S7. MF from the P-fc grid-search of one event of M_L=4.4; the meanings of the panels and symbols are the same as in Figure 7 of the main text. It is noteworthy that both (a) and (b) MF curves are characterized by a clear minimum. In (b) the MF curve bottoms at a lower value of RMS indicating that tomo Q corrections lead to an improved fit.

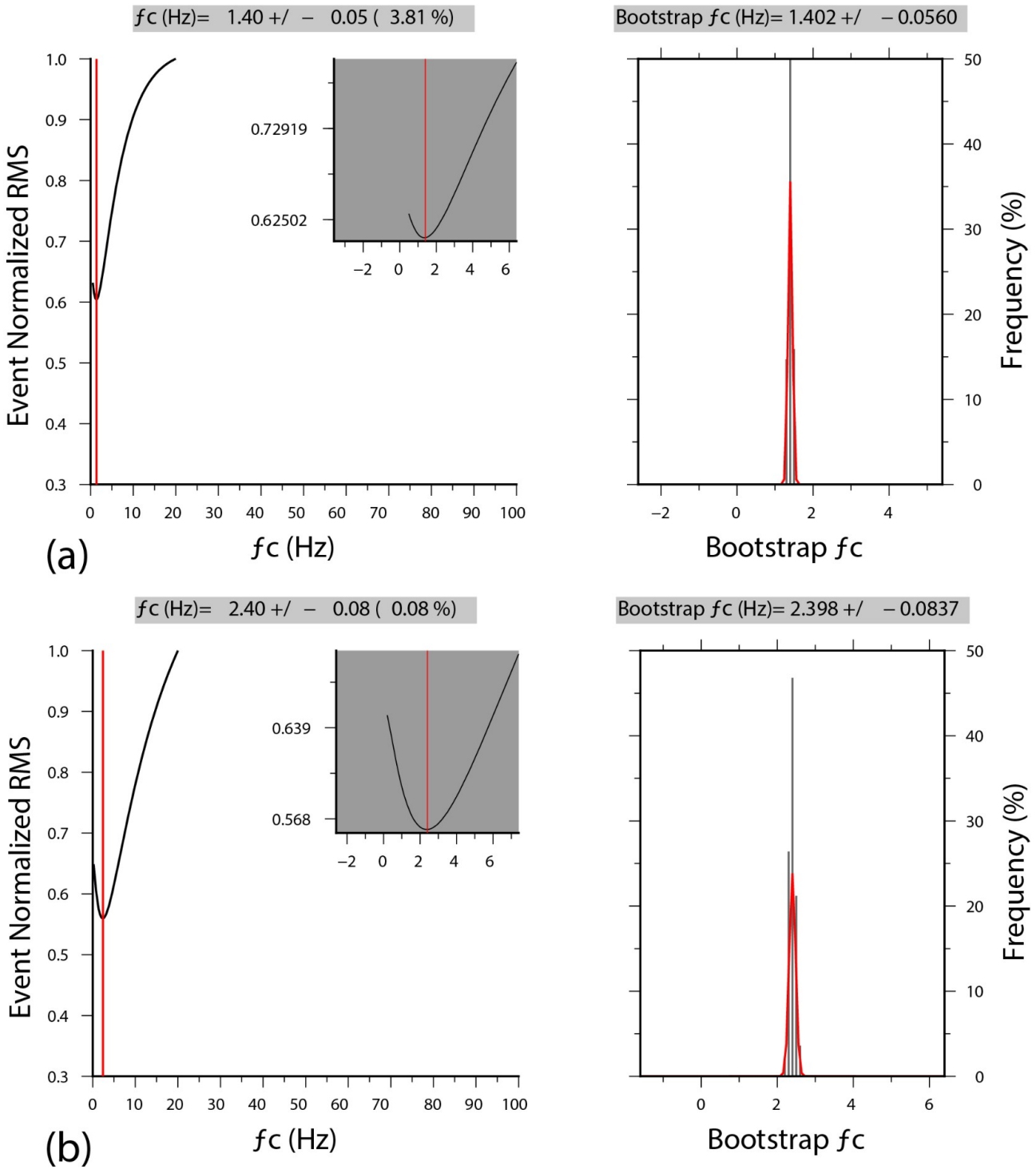

Figure S8 MF from the S-fc grid-search for the same M_L=4.4 event of Figure S7. The meanings of the panels and symbols are the same as in Figure 8 of the main text. It is noteworthy that both (a) and (b) MF curves are characterized by a clear minimum. In (b) the MF curve bottoms at a lower value of RMS indicating that tomo Q corrections lead to an improved fit.

5. Further assessment of the performance of our method by comparison w waves spectral ratio method

5.1 The Coda waves spectral ratio method.

This method, developed and described in detail by Yoshimitsu et al., 2019 (hereinafter YEA), relies on the use of the spectral ratio between two events of different magnitude but similar location. The smaller event acts as an EGF for the biggest one (BIG). The spectral ratio is used to remove from the BIG's spectrum the effect of path, attenuation and instrument that are quantified by the EGF spectrum. In such a way, the spectral ratio is only a function of the source characteristics of the pair of events. In the method of YEA, the signal that is used to compute the spectral content consists of a portion of the coda waves that conventional begin on seismograms at 2 times of the S-waves travel time (i.e. Herraiz and Espisosa, 1987). The definition of the BIG-EGF couple is essentially related to the inter-event distance and to the difference of magnitude between the events. In particular, the magnitude of BIG allows us to define a spatial volume and therefore the distance within which EGS must be located. Furtherly, the magnitude of BIG and EGF events must differ by at least 0.5. Following YEA, the spatial extent of the BIG event could be represented by the fault dimension estimated on the basis of the magnitude (see Kanamori and Anderson, 1975). A Mw 4 event, for example, is characterized by spatial length of 2 km. In this application, we apply the main steps described in YEA that, for sake of clarity, we summarize in the following points.

I) First, we form the couples of events by the approach based on the inter-events distances and magnitude differences. In our case we collect about 10,000 pairs of events with magnitude ranging from 2.0 to 4.0. We prefer to not include events with magnitude above 4 for these motivations: a) we are interested to follow strictly the recipes described in YEA where the maximum magnitude is 4; b) the use of M>4 force to use larger time windows that, especially in a seismic sequence, could be contaminated by later events.

II) We compute the spectra of coda waves at all the stations that have recorded the generic couple BIG-EGF, using the multiple time window described by YEA. For one station, a coda signal 10.24 s long is extracted on the 3 components of BIG and EGS waveforms, starting at twice the S wave arrival time. Along this portion of the seismogram, a 50% overlapping window of 5.12 is used to cut the signal and to compute the spectral content. Spectral amplitudes of the 3 resulting windows are then averaged and compared with the noise spectrum computed in a similar way by using the signal preceding the P onset. The signal spectrum is retained if the signal- to- noise ratio (SNR) is above 1.5 in the frequency-interval range from 0.2 to 20 Hz. The minimum frequency is related to the length of the moving window (5.12 s) while the maximum frequency is set on the basis of different trials. While YEA used 30 Hz as maximum frequency, in our case we are forced to reduce the analysis at 20 Hz. This necessity arises from the weakness of the coda signal from 20 to 30 Hz, probably due to the strong attenuation undergone by coda waves within the alluvial cover of Po plain.

III) For all the stations of the couple BIG-EGF and for all the components that pass the SNR selection, we compute the spectral ratio between BIG and EGF signal spectrum. We average all the single estimations obtaining the mean spectral ratio that represents the observed function to be fitted. Following equation (3) of YEA, the observed spectral ratio may be modeled by the function:

$$\frac{U1(f)}{U2(f)} = \frac{Mo1\,[1 + (f/fc\quad 2)^2]}{Mo2\,[1 + (f/fc\quad 1)^2]}$$

where $U_1(f)/U_2(f)$ is the observed ratio between BIG and EGF spectra, Mo_1, fc_1, Mo_2, fc_2 are seismic moment and corner frequency for BIG and EGF, respectively. The unknown parameters are fc_1, fc_2, and Mo_1/Mo_2. The fit is carried out by a grid-search that is tuned to find the global minimum by using the L2 norm of the residuals between observed and theoretical spectral ratio.

For fc we use a grid-search ranging from 0.2 Hz, the minimum frequency resolvable by the used time window (5.12 s), to 20 Hz, the maximum frequency that exceeds the noise level in our dataset. This range is then divided in 60 logarithmic equally spaced intervals to find the best fc_1 and fc_2. The same procedure is adopted to find the best Mo_1/Mo_2. In this case the extreme values where the grid-search runs are inferred by the observed spectral ratio values.

IV) After the determination of the spectral ratio fits, YEA suggests performing a fit selection based on the analysis of residual between observed and modeled spectral ratio. First, it should be verified that the residuals exhibit a gaussian-like distribution. This could be performed by the application of the Shapiro–Wilk (or Kolmogorov–Smirnov) statistical test. Second, it should be checked if residuals

present irregularities at some particular frequencies. Some irregularities may arise from the inadequacy of EGF to model path characteristics or by source-medium complexities. In the paper of YEA this quality control is performed by dividing the residual trends from 0.2 to 30 Hz into 5 overlapping segments. A residual trend is defined as regular if the sum of the absolute difference of the adjacent slopes is within a threshold set to 0.01. In our case, since the analyzed frequency range is smaller (0.2-20 Hz), we have to sensibly increase this threshold to account for more steep adjacent segments and a simple comparison with YEA is not straightforward. For this reason, we prefer to check the quality of our fits by using two additional methods. First, we use a simple comparison based on the cross-correlation coefficient (CC) between the observed and the modeled spectral ratio. After a visual inspection of our results we decided to choose only fit with CC > 0.90. Lower CC values are typically found when irregularities in the observed spectra ratio lead to unrealistic fit. Second, we use a bootstrap approach to quantify the stability of the computed parameters (f_{c_1}, f_{c_2}, Mo_1/Mo_2) as suggested in YEA. The residuals between the observed and the modeled spectral ratio, are randomly extracted and added to the synthetic curve to create a bootstrap sample. This bootstrap sample is then treated as a real case and the unknown parameters (f_{c_1}, f_{c_2}, Mo_1/Mo_2) are found. After 1,000 realizations, for each parameter we obtain a bootstrap distribution that allows estimates of mean value and standard deviation. We observe that when the observed spectral ratio is characterized by a regular sigmoidal shape, the fit is well constrained and the bootstrap distribution gives an average f_{c_1}, f_{c_2} estimations that are very close to the final fit. Finally, based on YEA and on the observation of our results, for a fit to be retained we impose that: 1) residuals between observed and modeled spectral ratio have a gaussian-like distribution, 2) the cross-correlation between observed and theoretical curve is at least 0.90, 3) the discrepancy between corner frequencies estimated by fitting the spectral ratio and those derived by the mean of the bootstrap distributions are within 1 Hz. These strong selection criteria furnish a total of 157 spectral ratio fit. In Figure S9 we show one example of these selected spectral ratios and, for comparison, in Figure S10, one discarded fit.

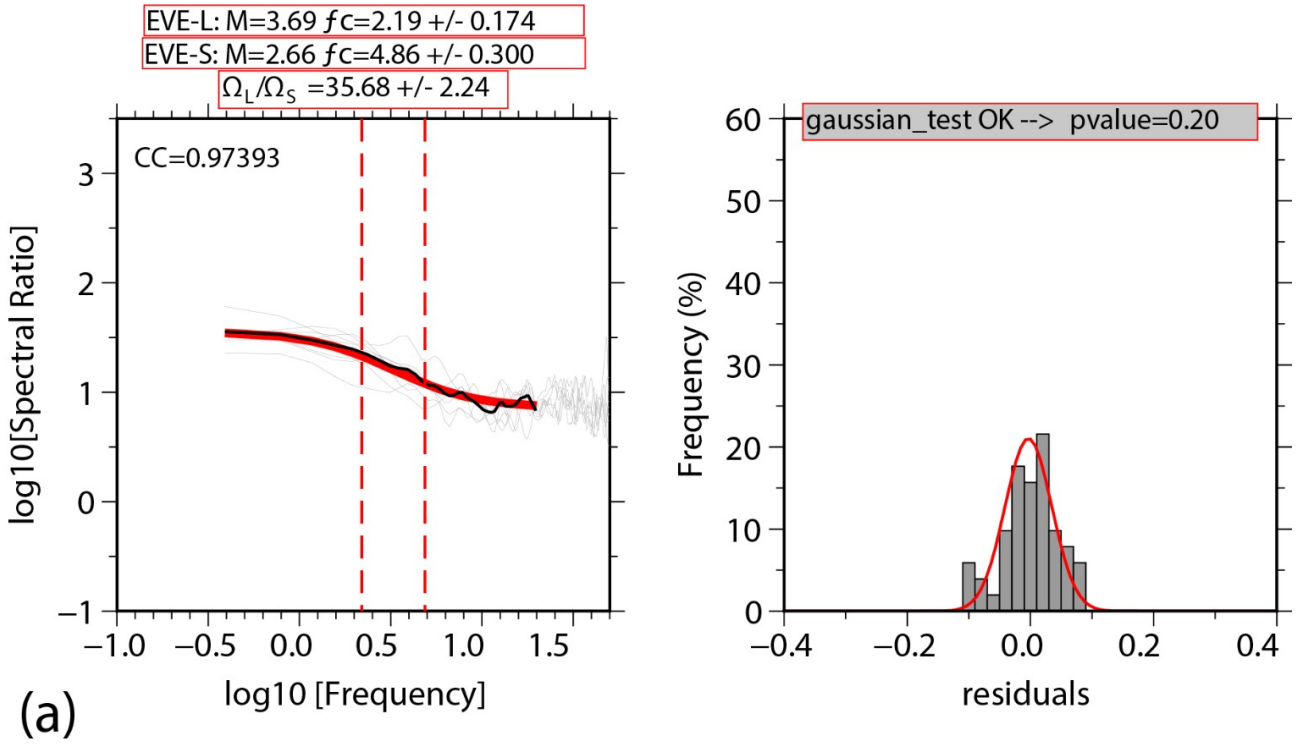
EVE-L: M=3.69 fc=2.19 +/- 0.174
EVE-S: M=2.66 fc=4.86 +/- 0.300
ΩL/ΩS =35.68 +/- 2.24
CC=0.97393
log10[Spectral Ratio]
log10 [Frequency]
gaussian_test OK --> pvalue=0.20
Frequency (%)
residuals
(a)

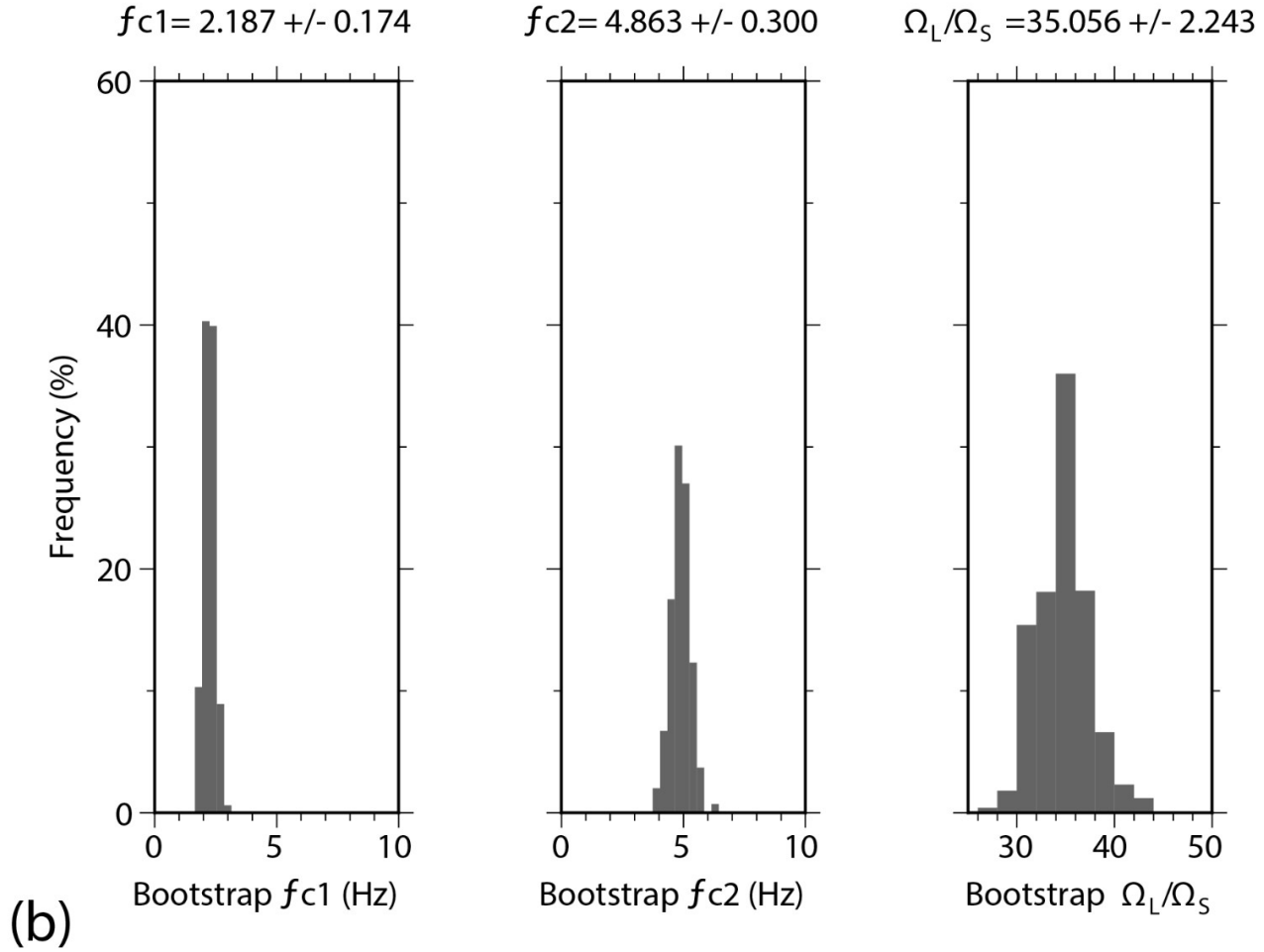
fc1= 2.187 +/- 0.174
fc2= 4.863 +/- 0.300
ΩL/ΩS =35.056 +/- 2.243
Frequency (%)
Bootstrap fc1 (Hz)
Bootstrap fc2 (Hz)
Bootstrap ΩL/ΩS
(b)

Figure S9. Example of the fitting procedure of spectral ratio that meets the selection criteria. (a) (left) spectra ratios of the available components (gray) and the averaging spectral ratio (black) that is fit by the red curve. Dotted vertical lines indicate the corner frequency for the largest and EGF events. The cross-correlation (CC) between observed and modeled spectral ratio is reported on the left corner. The title expresses the magnitude, the corner frequency and its bootstrap derived error for the larger event (EVE-L) and for EGF (EVE-S), respectively. (right) Histogram showing the residual distribution between observed and modeled spectral ratio. By the red color, the gaussian curve corresponding to the observed distribution is reported. As title we report the p-value that derives from the application of the Shapiro-Wilk test to explore the null hypothesis that the distribution of the residuals follows a normal distribution (if p-value > 0.05 we can assume that data are normally distributed). (b) Histograms showing the distribution of unknown parameters when we use the bootstrap approach to find the uncertainties on fc_1, fc_2, and Mo1/Mo2. When bootstrap distribution returns values of fc_1 and fc_2 within 1 Hz with respect to the fit results, we are confident that the fit is well constrained.

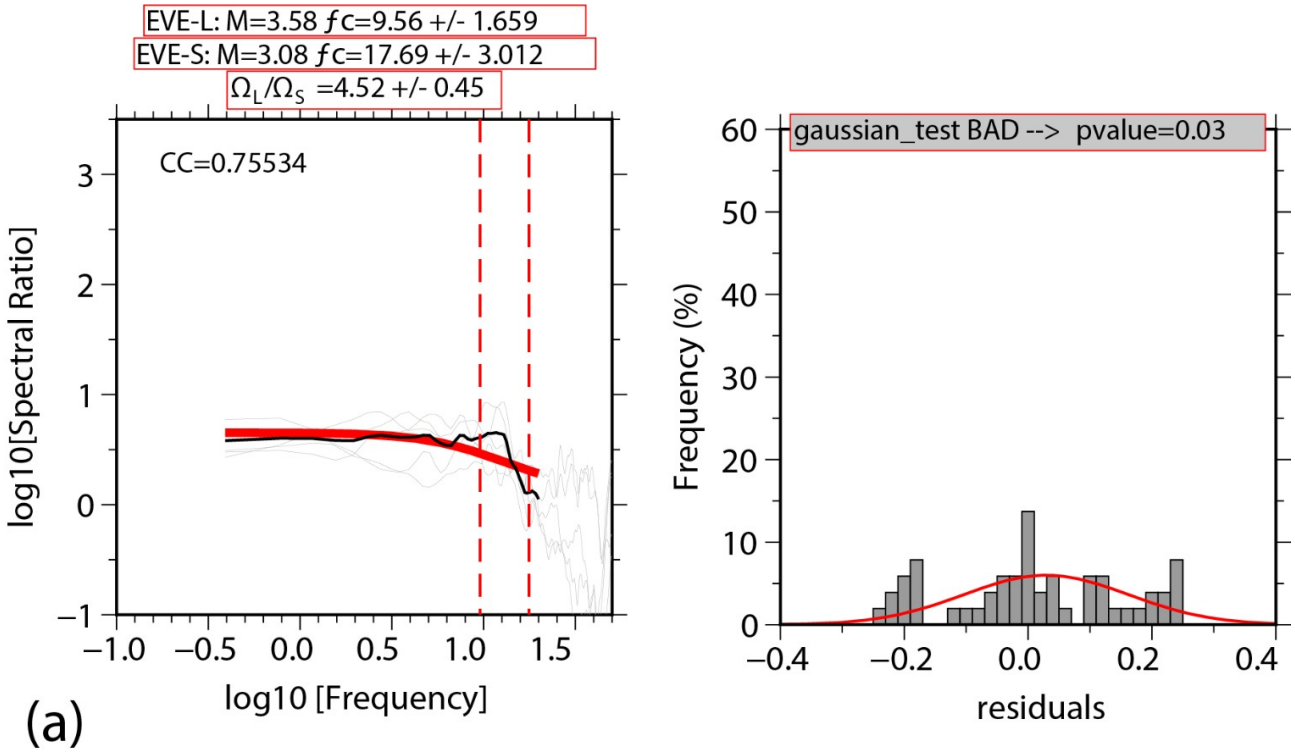
EVE-L: M=3.58 ƒc=9.56 +/- 1.659
EVE-S: M=3.08 ƒc=17.69 +/- 3.012
ΩL/ΩS =4.52 +/- 0.45
CC=0.75534
log10[Spectral Ratio]
log10 [Frequency]
gaussian_test BAD --> pvalue=0.03
Frequency (%)
residuals
(a)

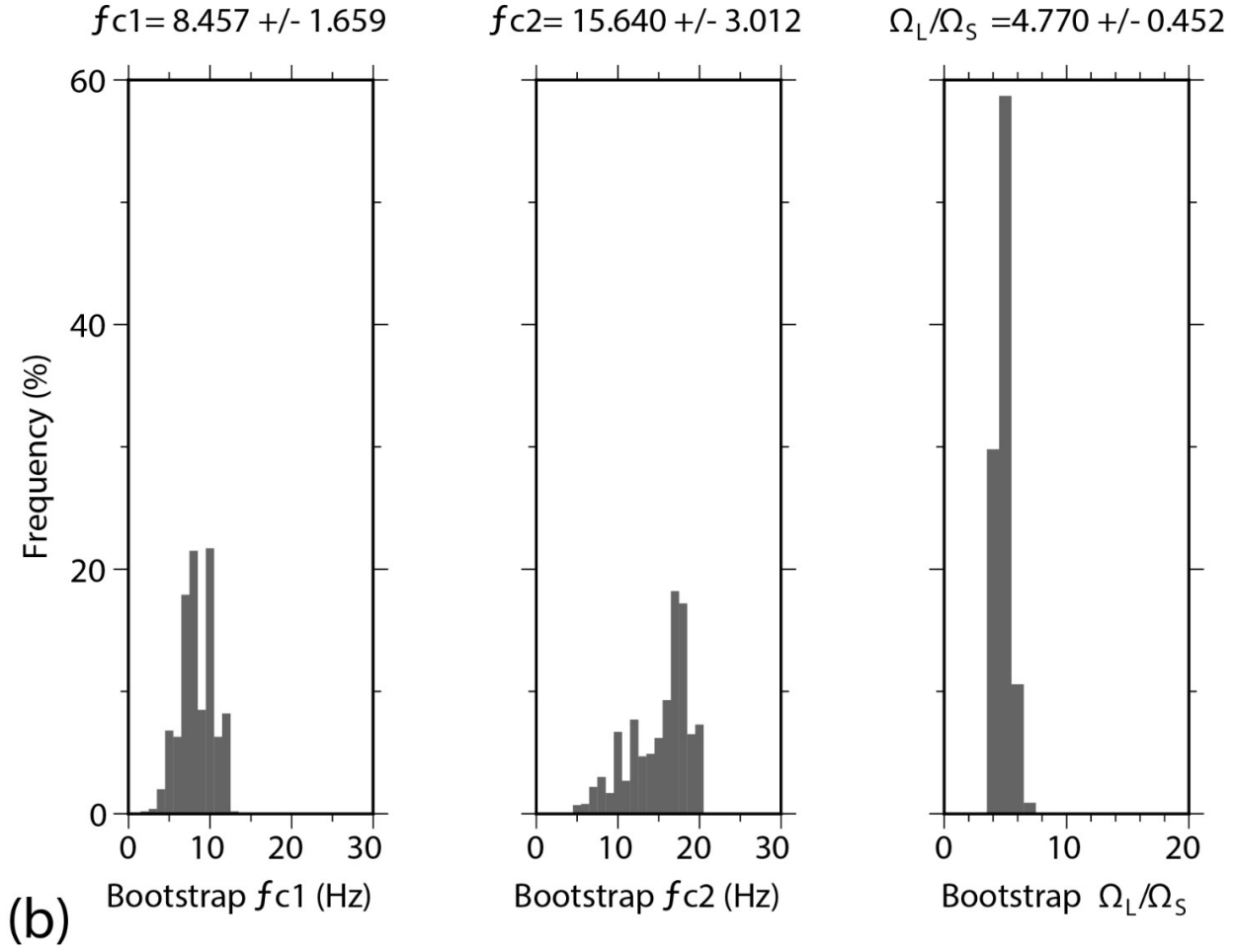
ƒc1= 8.457 +/- 1.659
ƒc2= 15.640 +/- 3.012
ΩL/ΩS =4.770 +/- 0.452
Frequency (%)
Bootstrap ƒc1 (Hz)
Bootstrap ƒc2 (Hz)
Bootstrap ΩL/ΩS
(b)

Figure S10. Example of the fitting procedure of spectral ratio that does not satisfy the selection criteria. See for details the caption of Figure S9. It is noteworthy that the bad quality of this fit is testified by low CC value and larger discrepancy between fit and bootstrap distribution corner frequencies.

V) For each selected fit, we first compute the absolute values of the seismic moment for the large and for the EGF event, starting from the computed ratio (Mo1/Mo2). For this purpose, we assume that the logarithmic average of seismic moments is equal to the value determined by the spectral fitting analysis (see Ide et al., 2003; Imanishi and Ellsworth 2006). Mo1 and Mo2 are then used with fc1 and fc2 to obtain an estimation of the static stress drop for the couple of events by using equation (7) of the main text, similar to the computation carried out for S-wave spectra.

VI) The couples of events are grouped to form clusters. A cluster is defined by couples of events that share the same largest magnitude event. We impose the minimum number of couples that populate a cluster to be 4. The spatial definition of each cluster depends on the spatial separation between the master and EGF event as specified at point I). Therefore, for the largest event, we obtain multiple estimations for fc and stress drop that are subsequently averaged to obtain robust estimations of such parameters. In Figure S11 we show an example of a cluster composed of 9 couples of events. For the master event, of M_L= 3.6, we obtain 9 estimations of fc and static stress drop that are averaged to obtain stable estimations of such parameters. The EGF events have only one estimate. However, if a generic EGF is shared with other clusters, averaged values could be determined similarly to the master event. For this cluster, master-event fc are between 3.5 and 4.8 Hz with an average value of 4.1+/-0.5 Hz (Figure S11a). EGF, having smaller magnitude, exhibits higher fc values (gray points in Figure S11a). If the couples of events are ordered as a function of the EGF magnitude (Figure S11b), we observe that EGF fc tends to decrease at increasing magnitude (Figure S11b). For the main event stress drop we obtain values between 7 and 12 Mpa with an average estimate of 9.6 +/–1.3 Mpa (Figure S11c), while EGF stress drops lie in the range 2-13 Mpa (Figure S11c). Sorting the same couples with EGF magnitude we observe that stress drop estimates do not show a clear trend (Figure S11d). In this case we can exclude that stress drops estimates are size dependent.

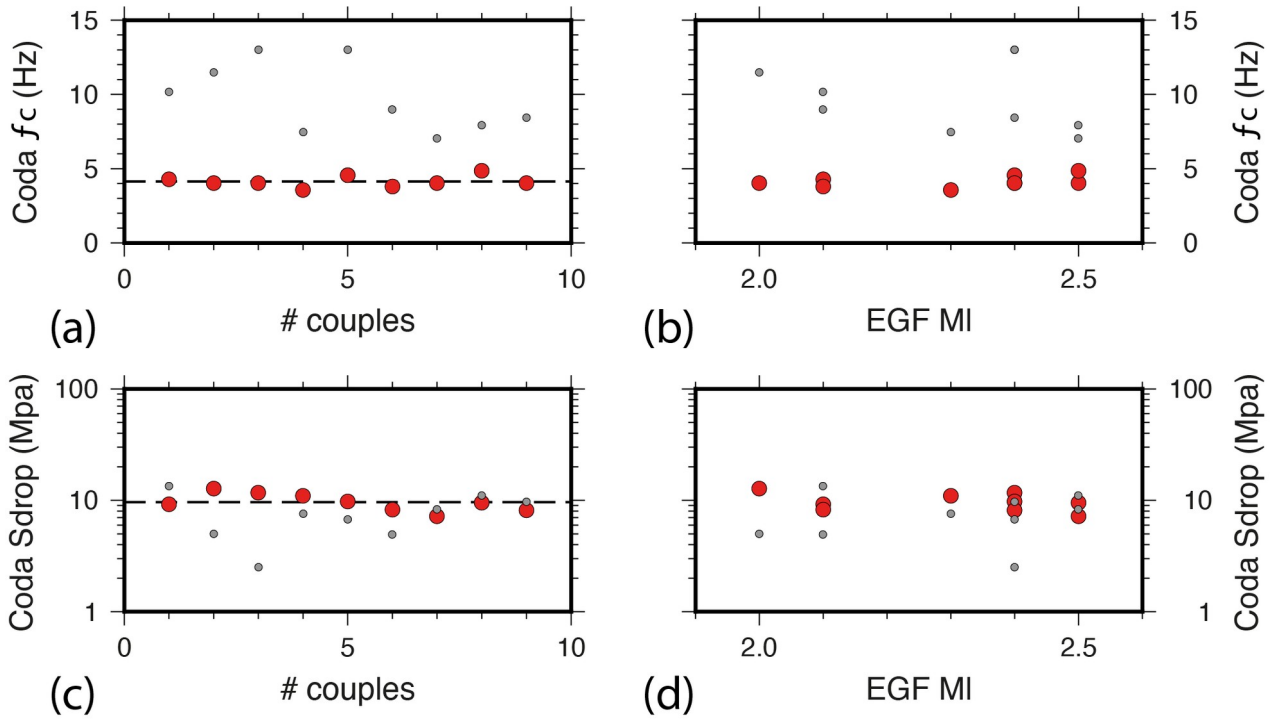

Figure S11: Characteristic of a generic cluster composed by 9 couples of events. The master event (M_L= 3.6) is common to all the 9 couples while the EGF events are different and are characterized by M_L ranging from 2.0 to 2.5. Red points indicate the estimations for the master events while gray points are representative of EGF. (a) fc for the master and the EGF events. Dotted line is the average fc for the master event. (b) fc for master-EGF events sorted by the EGF magnitude. (c) Stress drop estimates for master-EGF couples. Dotted line is the average stress drop for the master event. (d) Stress drop for master-EGF events sorted by the EGF magnitude.

5.2 Comparison of Stress-Drop estimations by spectral fit and coda-waves fit

The definition of clusters of events allows robust estimations of stress drop values for the master event. This is accomplished by averaging all the determinations obtained for each couple of events forming the cluster. In our case, we form clusters with at least 4 couples of events and therefore stress drop estimates of master events are computed by averaging at least 4 values. Performing the average stress drop between couples of events, that represents an important peculiarity of this method, leads to stable determinations of source parameters (see YEA). For EGF events, the robustness of stress drop determination depends on the number of couples to which such EGF belongs and therefore on the relative position with respect to the master events.

In the subsequent Figure S12 (already shown in the main text, as Figure 10), stress drop values determined for the cluster master events and for EGF shared with at least two large events, are

compared with stress drop estimated by the spectral fit procedure. From Figure S12a we observe that the points lay on the proximity of the equal-values line (gray line), showing a substantial agreement between the stress drop values determined by the two independent methods.

If we compare the stress drop variations computed with respect to the average value for the same pool of data, we observe that the majority of points fall in the NE-SW quadrants, delineating a positive correlation between stress drop variations. Since the average stress drop value is determined separately for coda and spectral fit data, this plot demonstrates that both stress drop datasets give equivalent indications about the variability of stress drop with respect to the mean value (Figure S12b).

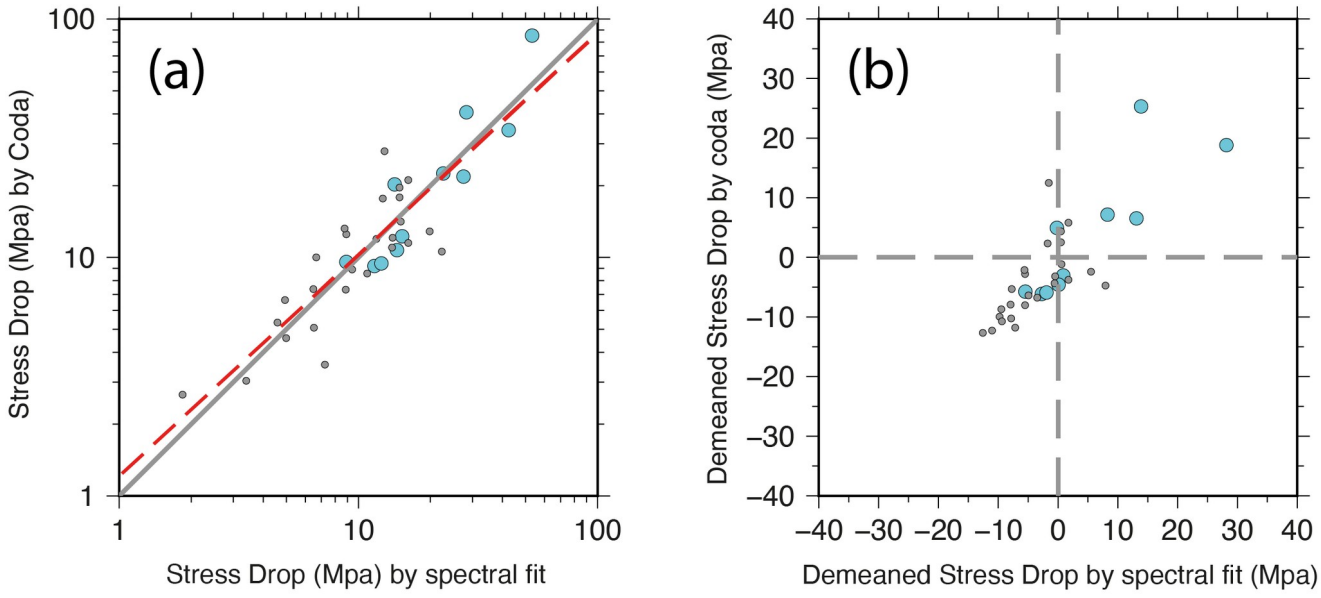

Figure S12. Comparison of Stress Drop computed by spectral fit and coda wave approach. Colored circles represent the master events of each cluster. The color is assigned on the basis of the magnitude as in Figure 4 (light blue= magnitude interval 3-4). Gray point represents EGF belonging to at least 2 clusters. (a) Comparison between absolute values of stress drop. The gray line indicates equal values of stress drop. The red dashed line represents the linear fit of data: slope = 0.87, intercept = 1.05. (b) Comparison of stress drop variation with respect to the mean value by using the same datasets of (a). Gray dashed lines indicate null variations with respect to the average stress drop.

References

Boatwright, J., J. B. Fletcher, and T. E. Fumal (1991). A general inversion scheme for source, site and propagation characteristics using multiply recorded sets of moderate-sized earthquakes, Bull. Seismol. Soc. Am. 81, 1754–1782.

Edwards, B., A. Rietbrock, J. J. Bommer, and B. Baptie (2008). The acquisition of source, path, and site effects from microearthquake recordings using Q tomography: Application to the United Kingdom, Bull. Seismol. Soc. Am. 98, 1915–1935.

Kanamori, H., and D. Anderson (1975). Theoretical basis of some empirical relations in seismology, Bull. Seismol. Soc. Am. 65, 1073–1096.

Koulakov, I., Bindi, D., Parolai, S., Grosser, H., and C. Milkereit (2010), Distribution of Seismic Velocities and Attenuation in the Crust beneath the North Anatolian Fault (Turkey) from Local Earthquake Tomography, Bulletin of the Seismological Society of America, Vol. 100, No. 1, pp. 207–224, February 2010, doi: 10.1785/0120090105

Herraiz, M., and F. Espinosa (1987). Coda waves: A review, Pure Appl. Geophys. 125, 500–577.

Ide, S., G. Beroza, S. Prejean, and W. Ellsworth (2003). Apparent break in earthquake scaling because of path and site effects on deep borehole recordings, J. Geophys. Res. 108, 2271, doi 10.1029/2001JB001617

Imanishi, K., and W. L. Ellsworth (2006). Source scaling relationships of microearthquakes at Parkfield, CA, determined using the SAFOD Pilot Hole seismic array, in Earthquakes: Radiated Energy and the Physics of Faulting, R. E. Abercrombie, A. McGarr, H. Kanamori, and G. Di Toro (Editors), American Geophysical Monograph 170, 81–90.

Rietbrock, A. (2001). P wave attenuation structure in the fault area of the 1995 Kobe earthquake, J. Geophys. Res. 106, 4141–4154.

Yoshimitsu, N., Ellsworth, W. L., Beroza, G. C. (2019). Robust stress drop estimates of potentially induced earthquakes in Oklahoma: Evaluation of empirical Green's function. Journal of Geophysical Research: Solid Earth, 124, 5854–5866. https://doi.org/10.1029/2019JB017483